Wind, Waves, and Fronts: Frictional Effects in a Generalized Ekman Model*

JACOB O. WENEGRAT

University of Washington, Seattle, Washington

MICHAEL J. MCPHADEN

NOAA/Pacific Marine Environmental Laboratory, Seattle, Washington

(Manuscript received 25 August 2015, in final form 15 November 2015)

ABSTRACT

Ocean currents in the surface boundary layer are sensitive to a variety of parameters not included in classic Ekman theory, including the vertical structure of eddy viscosity, finite boundary layer depth, baroclinic pressure gradients, and surface waves. These parameters can modify the horizontal and vertical flow in the near-surface ocean, making them of first-order significance to a wide range of phenomena of broad practical and scientific import. In this work, an approximate Green's function solution is found for a model of the frictional ocean surface boundary layer, termed the generalized Ekman (or turbulent thermal wind) balance. The solution admits consideration of general, more physically realistic forms of parameters than previously possible, offering improved physical insight into the underlying dynamics. Closed form solutions are given for the wind-driven flow in the presence of Coriolis–Stokes shear, a result of the surface wave field, and thermal wind shear, arising from a baroclinic pressure gradient, revealing the common underlying physical mechanisms through which they modify currents in the ocean boundary layer. These dynamics are further illustrated by a case study of an idealized two-dimensional front. The solutions, and estimates of the global distribution of the relative influence of surface waves and baroclinic pressure gradients on near-surface ocean currents, emphasize the broad importance of considering ocean sources of shear and physically realistic parameters in the Ekman problem.

1. Introduction

Diagnosing velocities in the ocean boundary layer is key to many issues of broad practical and scientific importance, from larval dispersion, to search and rescue, to the general ocean circulation. Today, much of our understanding of boundary layer currents remains rooted in classic Ekman theory, which holds that, with some knowledge of the turbulent eddy viscosity, the ageostrophic ocean response is completely determined by the surface wind stress (Ekman 1905). However, despite the tremendous explanatory power of Ekman theory, basic observational confirmation of the structure of flow in the boundary layer has been challenging.

In response to discrepancies between the theory and observations, a large literature has developed, focused on modifications to the classic Ekman theory. Broadly speaking, the proposed modifications to Ekman theory can be divided into local one-dimensional mechanisms, such as time variability (Price et al. 1986; Schudlich and Price 1998; Price and Sundermeyer 1999; McWilliams et al. 2009), vertical structure in eddy viscosity (Madsen 1977; Miles 1994; Grisogono 1995), or finite boundary layer depth (Welander 1957; Stommel 1960; Lewis and Belcher 2004; Elipot and Gille 2009), and mechanisms that involve nonlocal effects such as horizontal buoyancy gradients (McPhaden 1981; Cronin and Kessler 2009), surface waves (Huang 1979; Jenkins 1986; Xu and Bowen 1994; Lewis and Belcher 2004; Polton et al. 2005), and nonlinearity (Stern 1965; Niiler 1969; Thomas and Rhines 2002). Many of these proposed modifications have closed the gap between theory and observations; however, generally analytic solutions are only

* Joint Institute for the Study of the Atmosphere and Ocean Contribution Number 2465 and Pacific Marine Environmental Laboratory Contribution Number 4384.

Corresponding author address: Jacob O. Wenegrat, School of Oceanography, University of Washington, Box 357940, Seattle, WA 98195.
E-mail: wenegrat@uw.edu

DOI: 10.1175/JPO-D-15-0162.1

available for specific forms of parameters, limiting the possibility for intercomparison of the various proposed mechanisms and, critically, their application to realistic ocean fields.

Here we utilize a simple model of the viscous boundary layer, termed the generalized Ekman model (Cronin and Kessler 2009), or the turbulent thermal wind balance (Gula et al. 2014). This model contains many of the modifications to basic Ekman theory that have been proposed individually and has already proven successful in explaining observed horizontal currents (Cronin and Kessler 2009), as well as modeled boundary layer vertical velocities (Gula et al. 2014; McWilliams et al. 2015). Previously, solutions to this model with physically realistic parameters required numerical methods, with analytic solutions available only for greatly simplified forms of the parameters (Bonjean and Lagerloef 2002; Cronin and Kessler 2009; McWilliams et al. 2015), limiting insight into the underlying dynamics.

In this manuscript, we significantly extend these earlier results by providing an approximate solution to the generalized Ekman (turbulent thermal wind) model that can accommodate a wide range of physically realistic parameters, providing a unifying framework for many of the individually proposed modifications to classic Ekman theory (section 2). Using this solution, two limiting cases, corresponding to a surface wave field and a horizontal buoyancy gradient, are explored to further illuminate the underlying dynamics (section 3). The approximate solutions to these limiting cases reveal how these two ocean dynamic processes modify the Ekman solution in similar ways, drawing a previously unnoted connection between these processes and their accompanying literatures.

In section 4 the solution is applied to an idealized front, illustrating how thermal wind shear in the presence of viscosity can alter both the Ekman layer flow as well as drive overturning circulations in the boundary layer (Garrett and Loder 1981; Thompson 2000; McWilliams et al. 2015). Estimates of the global distribution of wave and baroclinic pressure gradient effects on frictional boundary layer flow (section 5) and scaling analysis suggest that these ocean dynamical processes can be expected to be of first-order importance in determining near-surface currents for much of the world's oceans.

2. Theory

We consider steady, Boussinesq flow in hydrostatic balance, where the complex horizontal velocity is denoted by $\mathbf{u} \equiv u + iv$, and $\nabla \equiv \partial/\partial x + i\partial/\partial y$. Horizontal mixing is ignored, and vertical mixing is parameterized by a turbulent eddy viscosity A_v, which is considered to be a specified parameter, allowed to vary vertically subject to moderate constraints imposed by the approximation technique utilized, as discussed below. The horizontal and vertical momentum equations are thus given by

$$if\mathbf{u} = -\frac{1}{\rho_0}\nabla P + \frac{\partial}{\partial z}\left(A_v\frac{\partial \mathbf{u}}{\partial z}\right), \quad \text{and} \tag{1}$$

$$0 = -\frac{1}{\rho_0}\frac{\partial P}{\partial z} + b, \tag{2}$$

where ρ is the density, the Rossby number $\varepsilon = U/fL$ is assumed small, and therefore the nonlinear advection terms are excluded. Equation (2) expresses the hydrostatic balance, where $b = -g\rho/\rho_0$ is the buoyancy, also considered to be a known quantity, allowed to vary in the horizontal and vertical.

Equation (1), a balance between the Coriolis acceleration, the pressure gradient force, and the turbulent diffusive flux convergence, provides the basic starting point for Ekman theory. Deriving Ekman's (1905) result begins with a decomposition of the total velocity into a geostrophic velocity in balance with the pressure gradient force [$\mathbf{u}_g = i(\rho_0 f)^{-1}\nabla P$] and solving for the ageostrophic velocity ($\mathbf{u}_a = \mathbf{u} - \mathbf{u}_g$) in a boundary layer with characteristic thickness $h_{\mathrm{Ek}} = \sqrt{2A_v/f}$, the Ekman depth, where it is assumed that A_v is vertically uniform and $\nabla b = 0$ (see, e.g., Gill 1982, section 9.6). Equation (1) is a second-order linear ordinary differential equation for velocity and so requires two boundary conditions on $\mathbf{u}$, given for the classic Ekman problem by $\rho A_v \partial \mathbf{u}_a/\partial z = \boldsymbol{\tau}_w$ at the surface, where $\boldsymbol{\tau}_w$ is the surface wind stress and $\mathbf{u}_a \to 0$ as $z \to -\infty$.

Here we take a more general approach that does not require separating into geostrophic and ageostrophic components by first vertically differentiating Eq. (1) and multiplying by $\rho_0 A_v(z)$ to form an equation for the stress $\boldsymbol{\tau} = \rho_0 A_v(z)\partial \mathbf{u}/\partial z$, which we refer to as the generalized Ekman model (following Cronin and Kessler 2009):

$$A_v(z)\frac{\partial^2 \boldsymbol{\tau}}{\partial z^2} - if\boldsymbol{\tau} = \rho_0 A_v(z)\nabla b, \tag{3}$$

$$\boldsymbol{\tau}(0) = \boldsymbol{\tau}_w, \quad \text{and} \tag{4}$$

$$\boldsymbol{\tau}(-h) = 0. \tag{5}$$

The relationship of this model to various alternate Ekman layer formulations is discussed in detail by Cronin and Kessler (2009); however, we further note that this is the same model termed the turbulent thermal wind balance by Gula et al. (2014) and McWilliams et al. (2015) in their investigations of submesoscale cold filament dynamics.

The surface boundary condition Eq. (4) is unchanged from the classic Ekman problem; however, the bottom boundary condition Eq. (5) is posed as a no-stress condition, applied at a finite depth $z = -h$, rather than the no-slip condition utilized in the classic Ekman problem. This formulation of the problem maintains the classic Ekman transport, even in the presence of geostrophic shear at the base of the layer (Cronin and Kessler 2009), and is applicable at low latitudes or in depth-limited seas (Stommel 1960; Bonjean and Lagerloef 2002). The solution technique utilized below is a global method, as opposed to a local boundary layer expansion, and thus sufficiently far from the boundary layer the solution will approach the inviscid limit. This gives a measure of flexibility in the choice of an appropriate h; however, on the basis of physical arguments, developed further below, h should be chosen to be deeper than significant sources of geostrophic stress (defined in section 3b), so as to avoid the creation of a spurious interior Ekman layer. When $h \gg h_{\mathrm{Ek}}$, as is the case for most of the extratropics, the near-surface solution is insensitive to the particular bottom boundary condition, and we further note that for the solutions given below, letting $h \to \infty$ results in simplified forms of the solutions that are equivalent to applying the bottom boundary condition $\boldsymbol{\tau} \to 0$ as $z \to -\infty$. However, if a no-slip boundary condition is desired, the derivation follows directly from that given in appendix A.

To solve this linear inhomogeneous ordinary differential equation with nonconstant coefficients, we first approximate a solution to the homogenous formulation of Eq. (3) using the Wentzel–Kramer–Brillouin (WKB) method (Bender and Orszag 1978; Grisogono 1995) and then solve for the inhomogeneous solution using variation of parameters (Hidaka 1955; Berger and Grisogono 1998). A detailed derivation of the full solution is presented in appendix A; however, briefly, the WKB method assumes the solution can be represented as

$$\tau \propto e^{(S_0+S_1\delta+S_2\delta^2+\cdots)(1/\delta)}. \tag{6}$$

Here, we use the physical optics approximation and solve to first order (S_1). The distinguished limit for the small parameter δ is found to be $\delta \sim \mathrm{Ek}^{1/2}$, where $\mathrm{Ek} = A_v/fH^2$, the Ekman number. The classic nondimensionalization of Eq. (1), for uniform A_v, identifies H as the depth scale of the interior flow, which for values typical of a stratified midlatitude ocean ($A_v \sim 10^{-2}\,\mathrm{m^2\,s^{-1}}$, $f \sim 10^{-4}\,\mathrm{s^{-1}}$, $H \sim 100\,\mathrm{m}$) gives $\mathrm{Ek} \sim O(10^{-2})$. However, retaining vertical structure in A_v introduces an additional vertical length scale h_{A_v} into the problem. We thus have six physically relevant terms (A_v, f, u_g, u_a, H, h_{A_v}), with two physical dimensions (time and length). Application of the Buckingham Pi theorem (Buckingham 1914) then gives four nondimensional parameters, two of which take the form of an Ekman number, $\pi_1 = A_{v0}/fH^2$ and $\pi_2 = A_{v0}/fh_{A_v}^2$. The latter of these is likely to be a stricter constraint on the validity of the WKB expansion when applied to realistic forms of A_v (appendix B).

Formally, the use of the WKB approximation requires that the properties of the medium vary more slowly than the solution (Bender and Orszag 1978), a condition that may be violated in some geophysical flows. Further analysis of this requirement is given in appendix A; however, as discussed in appendix B, we find good agreement between numerical and approximate solutions for a range of A_v profiles and values of Ek (see also Grisogono 1995), although we emphasize that care must be taken to assess the accuracy of the solution when applied to any specific A_v profile. For simplicity, we also require that $A_v > 0$ throughout the layer, so as to avoid the additional complexity of singularities in the equation. This constraint, and the WKB condition Eq. (A12), does not allow the direct application of the solution to cases where $A_v \to 0$ as $z \to 0$, a structure that is implied by the Monin–Obukhov similarity theory and that occurs in commonly utilized parameterizations such as the K-profile parameterization (KPP; Large et al. 1994). If necessary, this restriction can be removed by patching the WKB solution to an inner solution, valid in a thin layer as $A_v \to 0$, an example of which is given in appendix B. Despite these limitations, the simplicity and generality of the WKB method argue its utility, particularly in comparison to the often strict parameter requirements associated with other analytic solution techniques.

Once the WKB solution to the homogenous problem is identified, the inhomogeneous solution can be found using variation of parameters and stated in terms of a Green's function. The full solution (as derived in appendix A) is thus given by

$$\boldsymbol{\tau}(z) = \boldsymbol{\tau}_w \left[\frac{A_v(z)}{A_v(0)}\right]^{1/4} \frac{\sinh[\theta(z)]}{\sinh[\theta(0)]} + \int_{-h}^{0} G(z,s)[\rho_0 \nabla b]\, ds, \tag{7}$$

where

$$\theta(z) = \sqrt{if} \int_{-h}^{z} A_v(Z)^{-1/2}\, dZ, \tag{8}$$

and $G(z, s)$ is the symmetric Green's function,

$$G(z,s)=\begin{cases}\dfrac{\sinh[\theta(z)]\sinh[\theta(s)-\theta(0)]A_v(s)^{1/4}A_v(z)^{1/4}}{\sinh[\theta(0)]\sqrt{if}} & \text{if} \quad s>z,\\ \dfrac{\sinh[\theta(s)]\sinh[\theta(z)-\theta(0)]A_v(s)^{1/4}A_v(z)^{1/4}}{\sinh[\theta(0)]\sqrt{if}} & \text{if} \quad s<z.\end{cases} \tag{9}$$

This general solution is a primary result of this manuscript.

Velocity shear follows directly from the definition of stress. However, Eq. (3) is a third-order linear ordinary differential equation in velocity, and hence to go from shear to velocity requires an additional boundary condition. Here, to determine velocity we use the solution for stress directly in the momentum equation [Eq. (1)],

$$if\mathbf{u}=-\frac{1}{\rho_0}\nabla P+\frac{1}{\rho}\frac{\partial\boldsymbol{\tau}}{\partial z}, \tag{10}$$

where $\boldsymbol{\tau}$ is now known through Eq. (7). This approach ensures that the vertically integrated ageostrophic velocity satisfies the classic Ekman transport relation.

a. Wind-driven component

The wind-driven component of the stress is given by the first term on the RHS of Eq. (7), which can be compared to the exact solution for the case where A_v is vertically constant (Stommel 1960; Bonjean and Lagerloef 2002):

$$\boldsymbol{\tau}(z)=\boldsymbol{\tau}_w\frac{\sinh[\sqrt{if/A_v}(z+h)]}{\sinh(\sqrt{if/A_v}h)}. \tag{11}$$

The parallels between the WKB approximation Eq. (7) and the solution of the constant-A_v problem Eq. (11) are apparent, with the leading-order modification appearing in the argument of the hyperbolic functions $\theta(z)$ given by Eq. (8). This term can be understood as introducing a stretched vertical coordinate system, defined by the integral in Eq. (8) (Lupini et al. 1975). Accordingly, $h_{\mathrm{Ek}}(z)=\sqrt{2A_v(z)/f}$ defines a vertically localized Ekman depth, analogous to the local wavenumber found in WKB solutions to the wave equation (see, e.g., Gill 1982, section 8.12).

The amplitude of the stress is also modified by vertical variations in viscosity, which appears as a ratio to the one-fourth power. For a slowly vertically decaying A_v, the effect of this term will be apparent only as $z\rightarrow -h$, where the ratio of $A_v(z)/A_v(0)\ll 1$. Figure 1 compares example vertical profiles of stress and velocity for the case of A_v decaying exponentially with depth, and for constant A_v, to illustrate the modification of the vertical structure arising from retaining a depth-dependent A_v. This depth-dependent amplitude term allows the stress amplitude, and hence the ageostrophic velocity, to decay over a different vertical depth scale than the rotation of the stress vector, a feature that is commonly noted in observations but cannot be accommodated in classic Ekman theory (Price et al. 1986; Wijffels et al. 1994; Chereskin 1995; Price and Sundermeyer 1999). It is apparent that if A_v is vertically constant in Eq. (7), the standard solution [Eq. (11)], as originally identified by Stommel (1960) in an investigation of the dynamics of the equatorial undercurrent, is immediately recovered.

b. Inhomogeneous forcing

The second term on the RHS of Eq. (7) is a Green's function integral, which can accommodate arbitrary vertical structure in both ocean sources of stress, which appear as inhomogeneous forcing terms in Eq. (3), as well as in the profile of $A_v(z)$, subject only to the constraints imposed by the WKB method. The Green's function kernel takes the form of paired Ekman layers above and below interior sources of stress (Fig. 2), which demonstrates how ocean sources of shear in the presence of viscosity drive an ageostrophic frictional response felt throughout the entire boundary layer (Hidaka 1955; Csanady 1982). Far from the boundaries, the profile of the Green's function is symmetric above and below interior shear; however, approaching the boundaries of the domain the shape of the Green's function becomes increasingly asymmetric, and the integral contribution serves to satisfy the boundary conditions Eqs. (4) and (5).

The ageostrophic flow associated with several simplified forcings is shown in schematic form in Fig. 3. In the absence of wind stress, with vertically uniform A_v and ∇b, Ekman layers are generated, both at the surface as well as at the base of the boundary layer, to satisfy the boundary conditions (Bonjean and Lagerloef 2002). A more physically realistic case is given in Fig. 3b, where a vertically decaying buoyancy gradient gives rise to both a surface Ekman layer, as well as a diffuse interior ageostrophic flow. The strength of the interior portion of the flow, for the situation shown in Fig. 3b, scales as h_{Ek}/h relative to the surface ageostrophic flow and is therefore often assumed small and neglected. However, we note that this flow is necessary to balance the transport

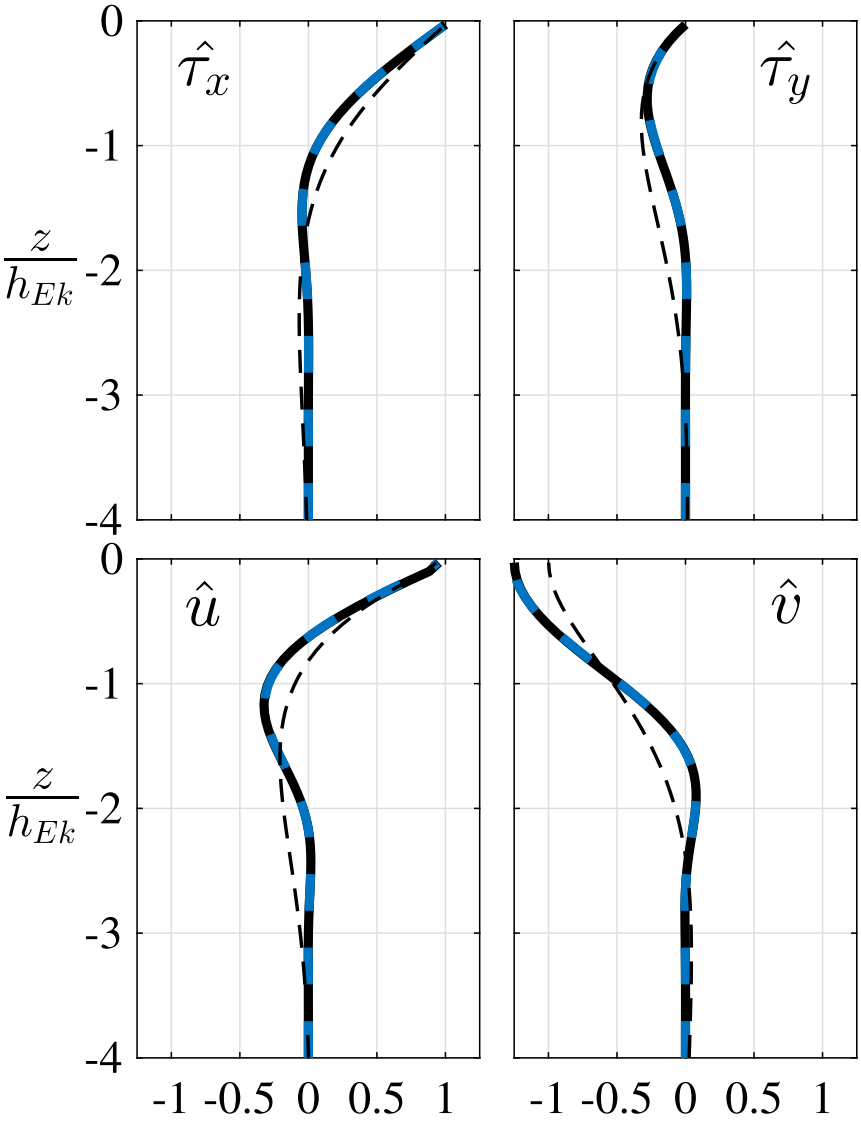

FIG. 1. Example profiles of stress and velocity for an exponentially decaying eddy viscosity $A_v = A_{v0}e^{z/h_{\mathrm{Ek}}}$ for numeric (solid black) and WKB solution given by Eq. (7) (dashed blue), and for constant eddy viscosity $A_v = A_{v0}$ (thin dashed black). (top) Stress profiles, normalized by the surface wind stress value $\hat{\boldsymbol{\tau}} = \boldsymbol{\tau}(z)/|\tau_w|$. (bottom) Velocity profiles, normalized by $\hat{\mathbf{u}} = \mathbf{u}(z)|\tau_w/[\rho f h_{\mathrm{Ek}}(0)]|^{-1}$. The WKB solution overlaps the numerical solution to within the thickness of the plotted line.

in the surface Ekman layer so as to maintain the classic Ekman transport relation. Further, this flow need not always be small, as illustrated in section 3a discussing surface wave effects, and hence should be retained. The final panel shows the case of a decaying A_v profile, with constant ∇b. The resulting ageostrophic velocities are similar to those in Fig. 3b; however, the associated buoyancy fluxes will differ between the two cases, emphasizing how horizontal fluxes will be a complex function of the spatial structure of both the background fields and A_v, discussed further in section 5b.

The total frictional ageostrophic response thus consists of a directly wind-forced component, as well as an integral over Ekman-like responses to interior shear. Therefore, in order to understand the oceanic response to wind forcing, it is also necessary to understand the ageostrophic frictional response to ocean dynamical processes (Cronin and Kessler 2009). Recent observational work has emphasized the importance of removing estimates of the geostrophic shear in order to isolate the ageostrophic flow (Chereskin and Roemmich 1991; Polton et al. 2013; Roach et al. 2015); however, the

analysis developed here suggests that to fully isolate the wind-driven component of this flow it is also necessary to account for ageostrophic flow driven by the geostrophic shear (section 3b). Further, although we have so far limited the discussion to shear that arises from baroclinic pressure gradients, we note that any other forcing terms in the momentum equations will act in a similar manner, and the case of Stokes shear from surface waves is discussed in section 3a. To further illustrate the underlying dynamical mechanisms, we now consider two limiting cases representing important sources of shear in the ocean surface boundary layer that admit further simplification of the full solution.

3. Limiting cases

a. *Stokes shear:* $h_s \ll h_{\mathrm{Ek}}$

Surface waves modify the oceanic boundary layer in a variety of important ways (Xu and Bowen 1994; McWilliams et al. 1997; McWilliams and Restrepo 1999; Sullivan and McWilliams 2010; Belcher et al. 2012; McWilliams et al. 2012). Here we focus on one particular aspect, termed the Coriolis–Stokes (CS) force, which appears as an additional term in the Eulerian momentum equation that arises from rotation acting on the Stokes drift, leading to a tilting of wave orbitals in the along-crest direction (Polton et al. 2005). The Coriolis–Stokes force has been shown to significantly modify flow in both the very near-surface layer, as well as throughout the entire Ekman layer (Huang 1979; Jenkins 1986; Lewis and Belcher 2004; Polton et al. 2005; Aiki and Greatbatch 2012; McWilliams et al. 2014).

Equation (1) can be rewritten to include the Coriolis–Stokes force as

$$if\,(\mathbf{u}+\mathbf{u}_s) = -\frac{1}{\rho_0}\nabla P + \frac{\partial}{\partial z}\left(A_v\frac{\partial \mathbf{u}}{\partial z}\right), \qquad (12)$$

with $\mathbf{u}_s$ as the Stokes velocity, given by $\mathbf{u}_s(z) = \int_k 2\sigma k\chi(k)e^{2|k|z}\,dk$, and where σ is the wave frequency, k is the wavenumber vector, and $\chi(k)$ is the directional wave spectrum (Huang 1971). We make the common simplifying assumption that $\mathbf{u}_s$ can be treated as a monochromatic wave such that $\mathbf{u}_s = U_0 e^{z/h_s}\hat{\mathbf{s}}(t)$, where $h_s = (2|k|)^{-1}$ and $\hat{\mathbf{s}}(t)$ is a unit vector in the direction of the waves, which is not necessarily aligned with the local surface wind stress. The wavenumber k and amplitude U_0 are assumed to be known or parameterized. It is important to note that for a time-varying wave field, the Coriolis–Stokes force initially accelerates an "anti-Stokes" flow (McWilliams and Fox-Kemper 2013), with transients that decay as $1/ft$ (Lewis and Belcher 2004). In the steady-state problem, including the Coriolis–Stokes force results in an additional forcing term on the RHS of Eq. (3), perpendicular to the wave direction, given by $if\rho A_v \partial \mathbf{u}_s/\partial z$. This appears in the full solution Eq. (7) within the Green's function integral, replacing the bracketed term with $[\rho\nabla b + if\rho\partial \mathbf{u}_s/\partial z]$. Hence, both horizontal buoyancy gradients and Stokes shear modify the standard Ekman solution in mathematically identical ways.

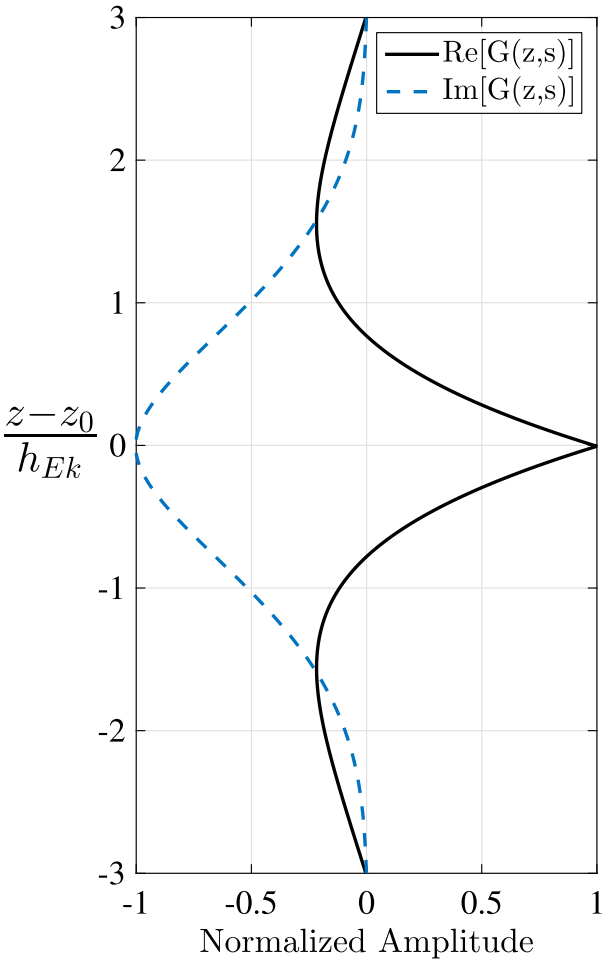

FIG. 2. Green's function [Eq. (9)] for a point source located at z_0 in a boundary layer of depth $h = 6h_{\mathrm{Ek}}$.

To provide an asymptotic approximation to Eq. (7), we can take advantage of the scale separation between the typical depth scale of the surface waves h_s, which is on the order of several meters, and h_{Ek}, which is on the order of tens of meters, such that $h_s \ll h_{\mathrm{Ek}}$. For simplicity in deriving the given form of Eq. (13), it is also assumed that $\boldsymbol{\tau}_{\mathrm{CS}}(-h) \sim 0$ and $h_{A_v} \gg h_{\mathrm{Ek}}$, where h_{A_v} is the depth scale over which A_v varies; however, neither of these assumptions are critical. After repeated integration by parts of Eq. (7), an asymptotic approximation is given by

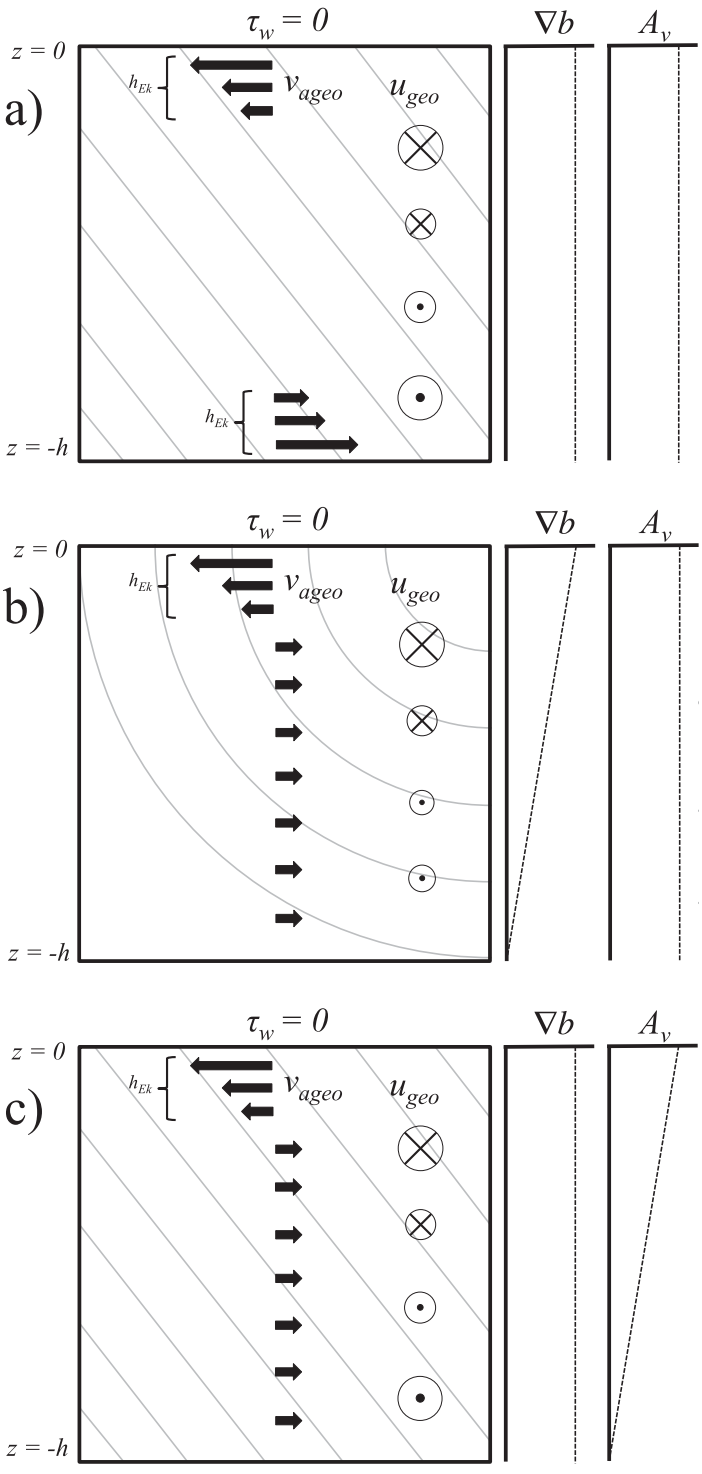

FIG. 3. Schematics of the ageostrophic flow induced by a horizontal buoyancy gradient, with thin lines indicating density contours. (a) Uniform viscosity and buoyancy gradient leads to a downgradient ageostrophic flow in the near-surface Ekman layer and upgradient flow in a bottom Ekman layer. (b) Uniform viscosity and linearly decaying buoyancy gradient leads to a downgradient ageostrophic flow in the Ekman layer and a uniform weak upgradient flow throughout the remainder of the layer. (c) Linearly decaying viscosity and uniform buoyancy gradient leads to a similar pattern of flow as in the middle panel. Figure is based on Thomas and Ferrari (2008, their Fig. 1).

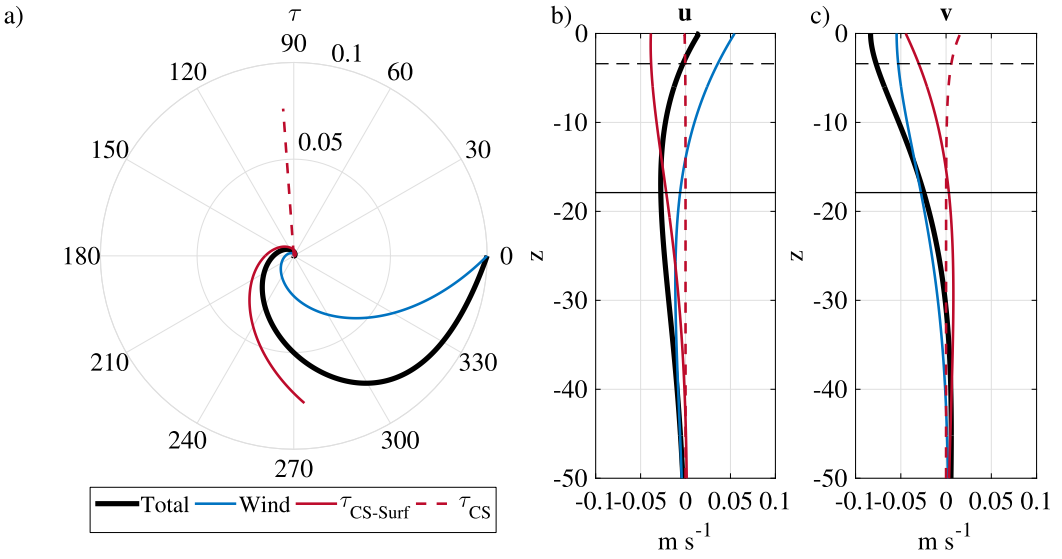

FIG. 4. Stress and ageostrophic velocity for a zonal surface wind stress $\tau_w = 0.1\,\mathrm{N\,m^{-2}}$ in the presence of a downwind wave field with Stokes velocity amplitude $U_0 = 0.22\,\mathrm{m\,s^{-1}}$ and depth scale $h_s = 3.4\,\mathrm{m}$ (Komen et al. 1996). (a) Hodograph of total stress (black), wind-forced component (blue), component forced by the effective surface stress arising from the Coriolis–Stokes stress (solid red), and the Coriolis–Stokes stress (dashed red). (b) Zonal ageostrophic velocity profile with components as in (a); (c) as in (b) but for meridional velocity. In (b) and (c) the Ekman depth (solid black) and h_s (dashed black) are indicated.

$$\boldsymbol{\tau}(z) \sim [\boldsymbol{\tau}_w - \boldsymbol{\tau}_{\mathrm{CS}}(0)]\left[\frac{A_v(z)}{A_v(0)}\right]^{1/4}\frac{\sinh[\theta(z)]}{\sinh[\theta(0)]} + \boldsymbol{\tau}_{\mathrm{CS}}(z),$$

$$\frac{h_s^2}{h_{\mathrm{Ek}}^2} \to 0. \tag{13}$$

The surface wave field therefore introduces a Coriolis–Stokes stress,

$$\boldsymbol{\tau}_{\mathrm{CS}}(z) = -\rho A_v \frac{\partial \mathbf{u}_s}{\partial z}\left[1 + i\frac{1}{2}\frac{h_{\mathrm{Ek}}^2(z)}{h_s^2}\right]^{-1}, \tag{14}$$

which is rotated $(90 + \Lambda)°$ to the left of the wave direction (Northern Hemisphere) where $\Lambda \sim \tan^{-1}(2h_s^2/h_{\mathrm{Ek}}^2)$ (Fig. 4). This stress modifies the ageostrophic frictional response in two ways. First, the Coriolis–Stokes stress can balance a portion of the applied surface wind stress, leading to a total Ekman layer response that can be considered as forced by an effective stress, given by the first bracketed term on the RHS of Eq. (13), rather than by the wind stress alone (Polton et al. 2005; McWilliams et al. 2014). Second, the Coriolis–Stokes stress directly affects a layer of depth scale h_s through the last term on the RHS of Eq. (13). The vertical divergence of this term, in Eq. (12), drives near-surface ageostrophic velocities that tend to rotate the surface flow into the down-wave direction (Figs. 4b,c). Together these two modifications introduce a boundary layer transport of $-U_0 h_s$, canceling the Lagrangian Stokes transport [see Polton et al. (2005) for a detailed discussion of the frictional Coriolis–Stokes transport].

The results of this section confirm the analysis of Polton et al. (2005) and extend them to an arbitrary vertical structure of A_v, subject to the aforementioned constraints (Song and Huang 2011). As discussed by Polton et al. (2005, their section 2c), Eqs. (13) and (14) imply that in the limit $h_s^2/h_{\mathrm{Ek}}^2 \to 0$, the wave modification to the Eulerian currents can be modeled solely through a modification to the surface boundary condition. The proceeding analysis confirms this result is fully independent of the particular form of vertical mixing and consequently may be of general use in guiding observational or modeling studies where the Stokes layer is not directly resolved.

b. *Thermal wind shear:* $h_{\mathrm{Ek}} \ll h_\rho, h_{A_v}$

A similar simplification of Eq. (7) can be found for the case of a horizontal buoyancy gradient driving a thermal wind shear in the near-surface layer. We assume that the Ekman depth is shallow relative to the depth scales over which the horizontal density gradient and A_v vary, that is, $h_{\mathrm{Ek}} \ll h_\rho, h_{A_v}$. An example of the scales associated with a mesoscale frontal system can be found from observations of the Azores front (Rudnick 1996), where, using parameters from Nagai et al. (2006), $h_{\mathrm{Ek}} \sim 15\,\mathrm{m}$; $h_{A_v} \sim 40\,\mathrm{m}$, based on the depth of the transition layer below the mixed layer; and $h_\rho \sim 100\,\mathrm{m}$, based on the depth of the thermocline and the observed geostrophic

frontal velocity. This limiting case is marginally valid for these parameter values and thus can be considered as requiring a fairly idealized frontal configuration (cf. Thomas and Lee 2005), included largely for the insight it offers into the basic dynamics of Eq. (7) and for comparison with Eq. (13).

For simplicity it is also assumed that $A_v \nabla b \to 0$ at $z = -h$. If this assumption is not made, the solution requires an additional bottom Ekman layer at $z = -h$ in order to satisfy the bottom boundary condition Eq. (5), as shown schematically in Fig. 3a. Repeated integration by parts of Eq. (7) leads to an asymptotic approximation given by

$$\boldsymbol{\tau}(z) \sim [\boldsymbol{\tau}_w - \boldsymbol{\tau}_{\text{geo}}(0)]\left[\frac{A_v(z)}{A_v(0)}\right]^{1/4}\frac{\sinh[\theta(z)]}{\sinh[\theta(0)]} + \boldsymbol{\tau}_{\text{geo}}(z), \quad \frac{h_{\text{Ek}}^2}{h_{\rho,A_v}^2} \to 0, \tag{15}$$

where

$$\boldsymbol{\tau}_{\text{geo}}(z) = \rho A_v \frac{\partial \mathbf{u}_g}{\partial z}\left\{1 - ih_{\text{Ek}}^2(z)\left[\frac{A_v'}{A_v}\frac{\nabla b'}{\nabla b} + \frac{1}{2}\frac{\nabla b''}{\nabla b} + \frac{3}{8}\frac{A_v''}{A_v} + \frac{3}{32}\left(\frac{A_v'}{A_v}\right)^2\right]\right\} \tag{16}$$

defines the geostrophic stress, with primes denoting vertical differentiation.

Closely paralleling the solution for the Coriolis–Stokes stress, Eq. (13), the modification of the surface boundary layer stress by horizontal buoyancy gradients also consists of two components. The first is a modification to the Ekman layer, whereby the Ekman response is forced only by that portion of the wind stress that is out of balance with the geostrophic stress, which again can be considered as defining an effective surface stress, given by the first bracketed term on the RHS of Eq. (15) (Thompson 2000; Nagai et al. 2006; Cronin and Kessler 2009). Thus, even in the case of $\boldsymbol{\tau}_w = 0$, thermal wind shear will drive an ageostrophic flow within the Ekman layer, with implications for frontal spin-down (Garrett and Loder 1981; Csanady 1982; Thompson 2000; Thomas and Rhines 2002), filament frontogenesis (Gula et al. 2014; McWilliams et al. 2015), and near-surface fluxes (Thomas and Ferrari 2008), discussed in section 5b. It is worth noting that advection of the horizontal buoyancy gradient by the ageostrophic frictional flow can modify the buoyancy gradient and thereby feed back into the Ekman solution, which is discussed in further detail in Thompson (2000) and McWilliams et al. (2015).

The second term on the RHS of Eq. (15) represents the turbulent stress that arises directly from a thermal wind shear in the presence of a viscosity, often termed the geostrophic stress, given by Eq. (16). The divergence of this term drives a weak flow throughout the entire layer with velocities that scale as h_{Ek}/h relative to the ageostrophic velocity in the Ekman layer, but with a vertically integrated transport that exactly cancels the transport in the Ekman layer driven by the surface geostrophic stress. The definition of geostrophic stress given here, Eq. (16), differs from that given by previous investigators, who, considering only vertically uniform A_v and ∇b, suggest $\boldsymbol{\tau}_{\text{geo}}(z) = \rho A_v(\partial \mathbf{u}_g/\partial z)$. Including vertical structure in these parameters gives rise to four additional terms in the definition of geostrophic stress, bracketed in Eq. (16), which enter the asymptotic approximation at order $h_{\text{Ek}}^2/h_{\rho,A_v}^2$.

These additional terms are imaginary and thus have the effect of rotating the geostrophic stress vector slightly from the geostrophic shear vector. This is illustrated in Fig. 5, where the geostrophic stress vector is rotated by an angle λ, which scales as $\lambda \sim \tan^{-1}(-h_{\text{Ek}}^2/h_{\rho,A_v}^2)$, or equivalently, $\lambda \sim \tan^{-1}(-2\text{Ek})$ (Fig. 6). Transport in the Ekman layer T_{Ek} is opposed by geostrophic-stress-driven transport over the full boundary layer depth T_{BL}. Surface velocity is given by $u_{\text{surf}} = u_{\text{Ek}}(0) + u_{\text{BL}}(0)$, a combination of the Ekman ageostrophic velocity forced by the effective surface stress (u_{Ek}) and an interior ageostrophic velocity forced by the divergence of the geostrophic stress (u_{BL}). The direction of the near-surface frictional flow relative to the buoyancy gradient is consequently a function of both the angle of the geostrophic stress, determined by vertical structure in A_v and ∇b, as well as the ratio $u_{\text{BL}}/u_{\text{Ek}} \sim h_{\text{Ek}}/h$. As a corollary to this, a latitudinal dependence in λ appears implicitly through the Ekman depth, as $h_{\text{Ek}}^2/h_{\rho,A_v}^2 \to \infty$ as $f \to 0$, with the geostrophic stress vector becoming increasingly parallel to the buoyancy gradient at low latitudes.

4. Frictional secondary circulation

The cross-front circulation that arises from frictional effects, shown schematically in Fig. 3, acts to spin down ocean fronts and sharpen cold filaments because of buoyancy fluxes associated with the ageostrophic velocities necessary to match the surface boundary condition Eq. (4) in the presence of a geostrophic shear (Garrett and Loder 1981; Thompson 2000; McWilliams et al. 2015). Further, in the case that $\nabla^2 b \neq 0$, convergences (divergences) of this cross-front ageostrophic

circulation will drive negative (positive) vertical velocities in the boundary layer (Garrett and Loder 1981; Thompson 2000). These effects have been examined primarily in the context of submesoscale dynamics, where the Rossby number ε is not small, and hence are generally diagnosed within the context of nonlinear models (e.g., Nagai et al. 2006). However, recent comparisons with modeled submesoscale eddies and filaments have suggested that vertical velocities in the boundary layer can be accurately diagnosed using this simple linear theory even at high ε (Ponte et al. 2013; Gula et al. 2014; McWilliams et al. 2015). At larger spatial scales, similar effects are also suggested in an ocean global climate model (Cronin and Tozuka 2015). Therefore, friction acting on the baroclinic component of the flow may be important to boundary layer dynamics across a range of spatial scales.

Vertical velocity for the generalized Ekman model is given by the standard relationship

$$w(x,y,z) = -\hat{\mathbf{k}}\cdot\nabla\times\frac{\boldsymbol{\tau}(x,y,z)}{\rho f} + L(x,y), \qquad (17)$$

where $L(x, y)$ is a constant of vertical integration chosen to fulfill a rigid-lid boundary condition. To illustrate how the various components of the full solution enter the calculated vertical velocity, we can utilize the simplified definition of stress given by Eqs. (13) and (15) in Eq. (17), which for a two-dimensional configuration, invariant in the y direction, reduces to

$$w(x,z) = -\frac{\partial}{\partial x}\left(\mathrm{Im}\left\{\frac{\boldsymbol{\tau}_{\mathrm{Eff}}(x)}{\rho f}\left[\frac{A_v(x,z)}{A_v(x,0)}\right]^{1/4}\frac{\sinh[\theta(x,z)]}{\sinh[\theta(x,0)]}\right\}\right) - \frac{\partial}{\partial x}\left\{\mathrm{Im}\left[\frac{\boldsymbol{\tau}_{\mathrm{Int}}(x,z)}{\rho f}\right]\right\} + L(x). \qquad (18)$$

The first term on the RHS represents upwelling occurring within the Ekman layer, which is now forced by an effective stress, $\boldsymbol{\tau}_{\mathrm{Eff}} = \boldsymbol{\tau}_w - \boldsymbol{\tau}_{\mathrm{CS}}(0) - \boldsymbol{\tau}_{\mathrm{geo}}(0)$. The second term on the RHS gives the boundary layer vertical velocity arising solely from the gradient of the interior forcing, $\boldsymbol{\tau}_{\mathrm{Int}} = \boldsymbol{\tau}_{\mathrm{CS}} + \boldsymbol{\tau}_{\mathrm{geo}}$. When Eq. (18) is evaluated at the base of the layer, $z = -h$, it reduces to the classic Ekman upwelling driven solely by the curl of the wind stress; however, within the layer, both horizontal gradients in the forcing and horizontal gradients of the vertical structure can drive vertical velocities. For the Ekman layer, this can be envisioned as Ekman transport occurring along contours of constant h_{Ek}, which, for a spatially varying A_v, have a vertical component.

Below the surface Ekman layer, where $\boldsymbol{\tau}_{\mathrm{CS}}(x, z) \approx 0$, and in the limit of $h_{\mathrm{Ek}}^2/h_{\rho,A_v}^2 \to 0$, Eq. (18) reduces to

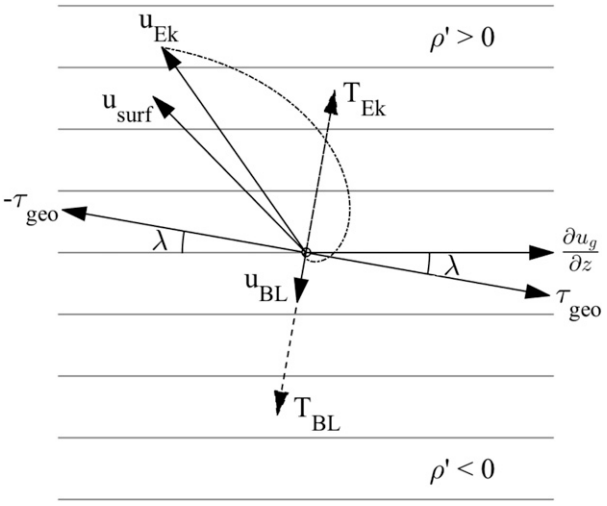

FIG. 5. Schematic of the components of the frictional ageostrophic response to a horizontal buoyancy gradient, with contours of constant ρ shown in gray. The geostrophic stress is rotated by an angle λ from the geostrophic shear, which points along lines of constant ρ. The divergence of this geostrophic stress drives an ageostrophic velocity u_{BL} and transport T_{BL}, rotated 90° to the right (Northern Hemisphere). Geostrophic stress at the surface drives an Ekman response, through an effective surface stress $-\tau_{\mathrm{geo}}$, with associated velocities u_{Ek} and transport T_{Ek}. The surface velocity is given by $u_{\mathrm{surf}} = u_{\mathrm{BL}}(0) + u_{\mathrm{Ek}}(0)$. Vectors are not to scale.

the scaling given by Garrett and Loder (1981), $w \sim gf^{-2}\rho^{-1}\partial(A_v\partial\rho/\partial x)/\partial x$. Thus, vertical velocity in the boundary layer interior, outside the Ekman layer, is driven by gradients in thermal wind shear and A_v, with order $h_{\mathrm{Ek}}^2/h_{\rho,A_v}^2$ modifications due to the gradient of the bracketed terms in Eq. (16), reflecting the role of the vertical structure of A_v and ∇b in setting the direction of the geostrophic stress vector (section 3b, Fig. 6). Approaching the surface, vertical velocity decays exponentially over an Ekman layer of depth scale h_{Ek}, with additional near-surface vertical velocities in a thin layer of depth scale h_s driven by the Coriolis–Stokes stress.

To illustrate the secondary circulation that arises from the balance Eq. (1), we examine an idealized front in the x–z plane (200-km width, h = 500 m), based on an approximation of the Frontal Air–Sea Interaction Experiment (FASINEX) data (Pollard and Regier 1992), similar to Thompson (2000). We set $\boldsymbol{\tau}_w = 0$ and $\boldsymbol{\tau}_{\mathrm{CS}} = 0$, as the solution is linear and these effects are simply additive. The buoyancy in this model is given by

$$b(x,z) = \frac{1}{2}b_f\tanh\left[\frac{\hat{z} - \alpha(\hat{x}-x_0)^3 - z_0}{d_0}\right] + \frac{1}{2}b_b\tanh\left[\frac{\hat{z}-z_0}{d_1}\right], \qquad (19)$$

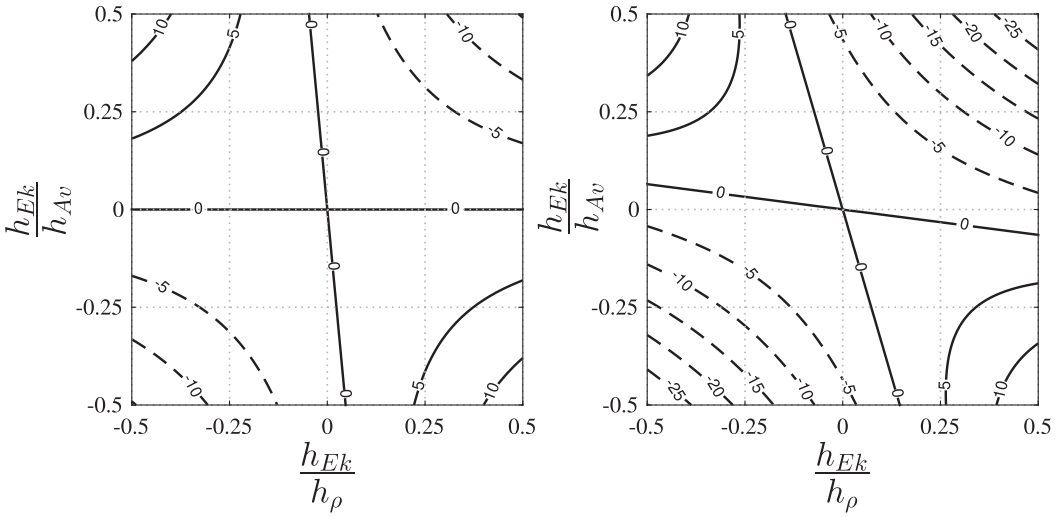

FIG. 6. Contour plots of λ (°, positive solid, negative dashed), the angle of the geostrophic stress relative to the direction of the geostrophic shear, as defined in the text by Eq. (16), evaluated at $z = 0$. (left) Linear A_v [$A_v(z) = A_{v0}(1 + z/h_{A_v})$] and linear ∇b [$\nabla b(z) = B_0(1 + z/h_\rho)$]. (right) Modified Gaussian A_v {$A_v(z) = A_{v0}[(z/h_{A_v}) + 0.25]\exp[-1/2(z/h_{A_v})^2 + 1/2]$}, as discussed in appendix B, and exponential $\nabla b(z)$ [$\nabla b(z) = B_0 e^{z/h_\rho}$]. In both plots positive parameter values indicate fields that decay downward.

with values of parameters given in Table 1 and the hat notation indicating nondimensionalized coordinates ranging from 0 to 1. Values of A_v are based on the approximation used in McWilliams et al. (2015), designed to be broadly consistent with KPP (Large et al. 1994). This is used simply to illustrate several general features of the solution that arise from horizontal and vertical structure in mixing across a frontal region, rather than to provide an absolutely accurate diagnostic, and the qualitative discussion that follows is not sensitive to the detailed particulars of our choice of A_v:

$$A_v(x,z) = A_{v0}G(\zeta)\frac{\hat{h}(\hat{x})}{h_0} + A_{vb}, \quad \zeta = -\frac{\hat{z}}{\hat{h}(x)}, \tag{20}$$

$$G(\zeta) = \frac{27}{4}(1+\zeta_0^2)(\zeta_0+\zeta)(1-\zeta)^2, \quad \zeta \le 1, \quad \text{and} \tag{21}$$

$$G(\zeta) = 0, \quad \zeta > 1. \tag{22}$$

The variable G has a maximum value of ~1 in the boundary layer, ζ_0 is a small parameter introduced to avoid a singularity at $z = 0$, and $\hat{h}$ is the surface boundary layer depth, taken here as

$$\hat{h}(x) = h_0 + \delta_h\left\{\tanh\left[\frac{\alpha(\hat{x}-x_0)^3}{d_0}\right] - \frac{1}{2}\right\}. \tag{23}$$

All parameter values for Eqs. (19)–(23) are given in Table 1. Figure 7 shows the structure of the idealized

TABLE 1. Parameters for Eqs. (19)–(23).

Parameter	Value	Physical interpretation
b_f	$-0.6g/\rho_0$	Buoyancy change across front
b_b	$b_f/2$	Buoyancy change across thermocline
α	-1.185	Horizontal scaling factor
z_0	0.75	Vertical position
x_0	1	Horizontal position
d_0	0.125	Horizontal scale
d_1	0.125	Vertical scale
f	$6.88 \times 10^{-5}\,\mathrm{s}^{-1}$	Coriolis frequency
A_{v0}	$3 \times 10^{-2}\,\mathrm{m}^2\,\mathrm{s}^{-1}$	Eddy viscosity magnitude
A_{vb}	$1 \times 10^{-4}\,\mathrm{m}^2\,\mathrm{s}^{-1}$	Background viscosity
h_0	0.84	Turbulent boundary layer depth
δ_h	0.05	Across front change in boundary layer depth
ζ_0	5×10^{-3}	Regularization constant

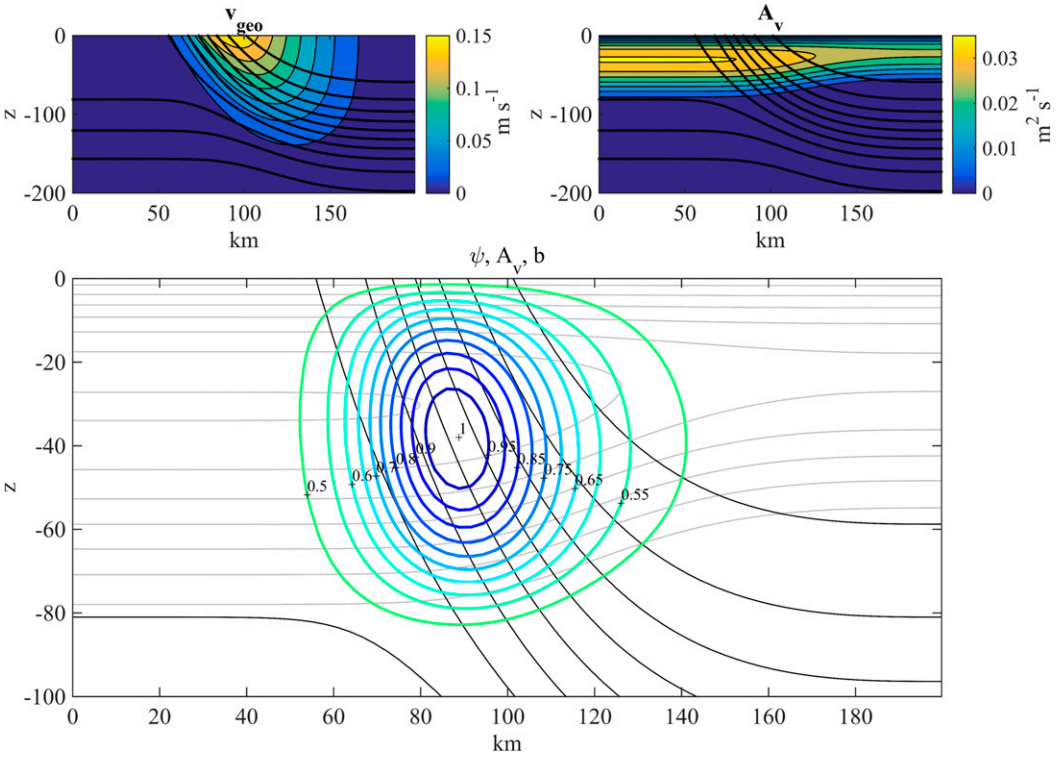

FIG. 7. Across-front sections of the idealized two-dimensional front discussed in section 4, with contours of constant ρ indicated in solid black. (top left) Along-front geostrophic velocity, (top right) A_v, and (bottom) frictional ageostrophic overturning streamfunction [$m^2 s^{-1}$; Eq. (24)], with contours of constant A_v in gray.

front and the eddy viscosity, along with the associated along-front geostrophic flow, implying $\varepsilon \sim 0.05$. We further assume $w = 0$ at $z = 0$ (rigid lid) and define an ageostrophic cross-front streamfunction such that $(u_a, w) = (\psi_z, -\psi_x)$. Using the meridional momentum equation, Im [Eq. (1)], gives

$$\psi = \frac{1}{\rho f}\tau^y(x,z). \tag{24}$$

The secondary overturning circulation arising from the geostrophic stress is found numerically and is shown in Fig. 7. This is a thermally direct circulation with a counterclockwise sense of rotation that tends to tilt the front and restratify the near surface (Thompson 2000). Downwelling velocities on the dense side of the front are stronger than the upwelling on the buoyant side of the front, consistent with previous findings (Samelson 1993; Thompson 2000). Streamlines are closed, indicating zero vertically integrated horizontal transport, as required to maintain the classic Ekman transport. This is a general result that does not depend on the frontal configuration. Note, however, that although the vertically integrated horizontal transport is zero, the associated fluxes need not be zero, as discussed further in section 5b. Furthermore, the vertical buoyancy flux associated with the secondary overturning circulation can be nonzero (McWilliams et al. 2015) and hence may play a role in the general circulation through vorticity stretching of the interior.

To illustrate the importance of spatial variability in A_v, we decompose the total vertical velocity field (Fig. 8a) w_{total} into vertical velocities due to the gradient in the forcing ($\nabla^2 b$), which we designate w_{forcing}, and the remainder that is a function only of the spatial structure in A_v, which we designate w_{A_v}, as discussed in relation to Eq. (18). For the particular frontal configuration examined here, w_{A_v} is ~25% of w_{total}. However, locally near the base of the turbulent boundary layer (Fig. 8, dashed line) w_{A_v} can be the dominant term and hence may be of particular importance for vertical fluxes into the near-surface layer. For a geostrophic stress, the ratio of vertical velocities is given by

$$\frac{w_{A_v}}{w_{\text{forcing}}} \sim \frac{L_{\text{forcing}}}{L_{A_v}}, \tag{25}$$

where L indicates the relevant horizontal length scales. Observations suggest that horizontal length

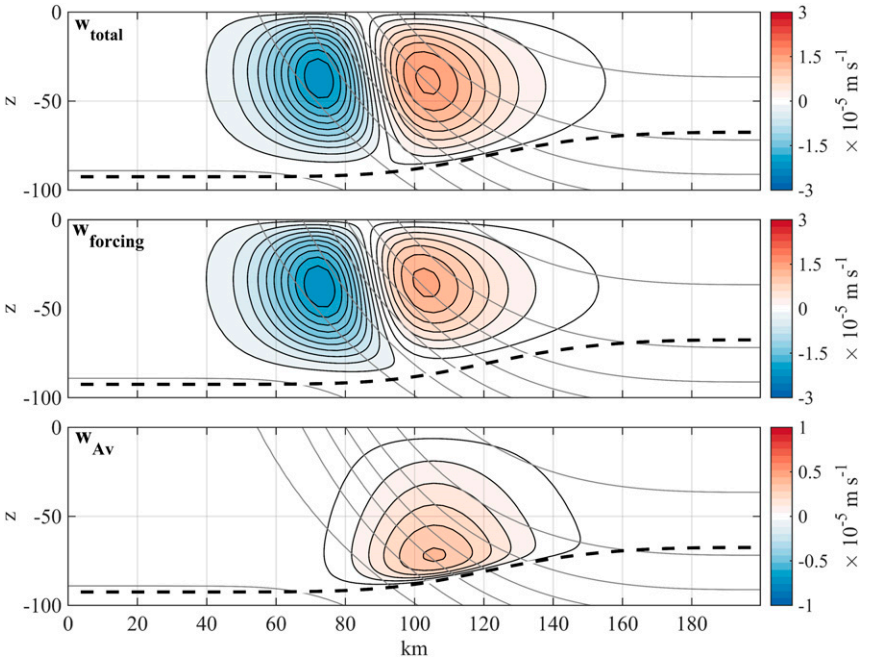

FIG. 8. Frictionally driven boundary layer vertical velocity. (top) Total vertical velocity, (middle) vertical velocity arising from the gradient in the horizontal buoyancy gradient, and (bottom) vertical velocity due to gradient in A_v. The dashed line indicates the turbulent surface boundary layer depth, defined by Eq. (23). Note reduced color scale in bottom panel.

scales over which vertical mixing varies are comparable to frontal features (Dewey and Moum 1990; Nagai et al. 2006), and thus these effects may be first order in determining the vertical velocity in the boundary layer. A similar scaling holds within the Ekman layer, where for a surface wind stress aligned orthogonal to a horizontal gradient in A_v, the ratio of vertical velocities at $z = -h_{\mathrm{Ek}}$ is

$$\frac{w_{A_v}}{w_{\mathrm{forcing}}} \sim \frac{L_{\mathrm{forcing}}}{4L_{A_v}}. \tag{26}$$

5. Discussion and further implications

The solutions presented here build upon prior work by allowing vertical variation in A_v, as well as realistic structure in ocean fields, such as ∇b and the Coriolis–Stokes force. Examination of the solutions [Eqs. (7), (13), and (15)], suggests many ways in which including more physical realism in the problem parameters can modify the expected ageostrophic flow; however, to further motivate the importance of this added complexity, we first consider scaling arguments relating the importance of geostrophic stress and Coriolis–Stokes stress to wind stress. The global distribution of these fields is then estimated using a combination of model output and reanalysis data. Finally, we comment briefly on the importance of these modifications to determining horizontal fluxes in the boundary layer.

a. Scaling and geographic distribution

The boundary conditions utilized here ensure that the classic Ekman transport relation is maintained, even in the presence of ocean sources of stress. However, as demonstrated in section 2, ocean sources of stress can greatly modify the vertical structure of currents and hence are fundamental to understanding boundary layer dynamics. Determining the magnitude of both the geostrophic stress and the Coriolis–Stokes stress depends critically on the value of A_v, which complicates their determination from observations. However, at low frequencies, variability in near-surface A_v may be controlled by variability in the surface wind stress (Wenegrat et al. 2014). Taking $h_{\mathrm{Ek}} \sim u_*/f$ (Caldwell et al. 1972), where $u_* = \sqrt{\boldsymbol{\tau}_w/\rho}$, gives $A_v \sim u_*^2/f$, and hence the ratio of the geostrophic stress to the surface wind stress can be scaled as

$$\gamma_{\mathrm{GEO}} = \frac{\boldsymbol{\tau}_{\mathrm{geo}}}{\boldsymbol{\tau}_w} \sim \frac{\nabla b}{f^2}. \tag{27}$$

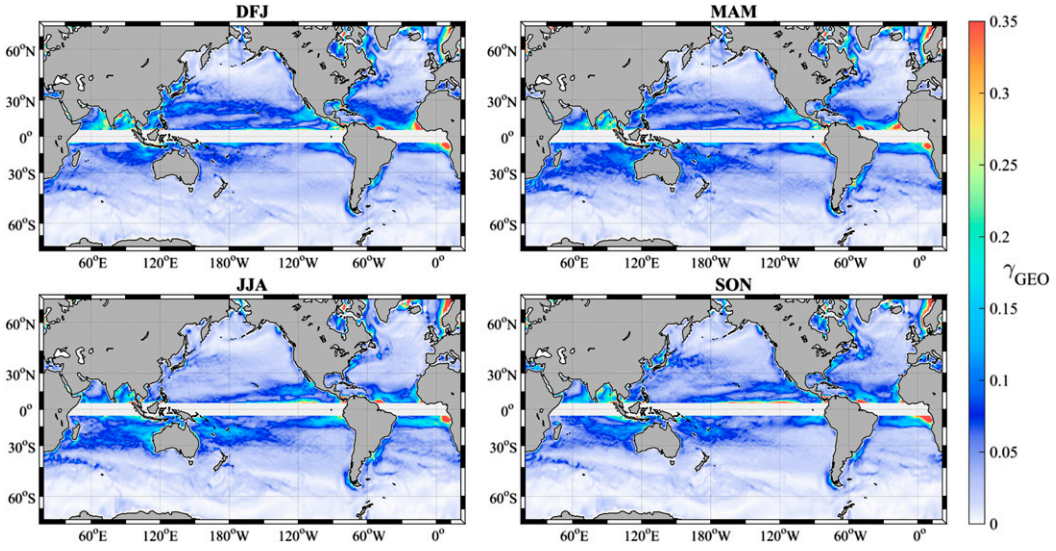

FIG. 9. Global climatology from 2001–11 by seasons, with months indicated in plot titles, for γ_{GEO} as defined in the text by Eq. (27).

The direct proportionality of γ_{GEO} to ∇b, and independence from $\boldsymbol{\tau}_w$, highlights how the geostrophic stress can be expected to be a ubiquitous forcing of ageostrophic flow at sharp frontal features and consequently may be fundamental for understanding horizontal heat flux at buoyancy fronts. The f^{-2} dependence indicates a rapid increase at low latitudes. Further, utilizing the stratified Ekman depth scaling $h_{Ek} \sim u_*/\sqrt{Nf}$ (Pollard et al. 1972) in Eq. (27) gives $\gamma_{GEO} \sim$ Bu, where Bu $= NH/fL$ is the Burger number, defined such that $b \sim N^2 H$. Determination of Bu is thus dependent on the geometry of the particular front being considered; however, for many oceanic flows observations suggest Bu $\sim O(1)$, implying $\gamma_{GEO} \sim O(1)$ (Nagai et al. 2006; Boccaletti et al. 2007).

The Coriolis–Stokes stress can be scaled relative to the surface wind stress as

$$\gamma_{CS} = \frac{\tau_{CS}}{\tau_w} \sim U_0 h_s \frac{\rho f}{\tau_w} \sim \mathrm{La}^{-2} \frac{h_s}{h_{Ek}}. \tag{28}$$

Therefore, γ_{CS} is proportional to the Stokes transport divided by the wind-driven Ekman transport (McWilliams and Restrepo 1999; Polton et al. 2005). Alternatively,

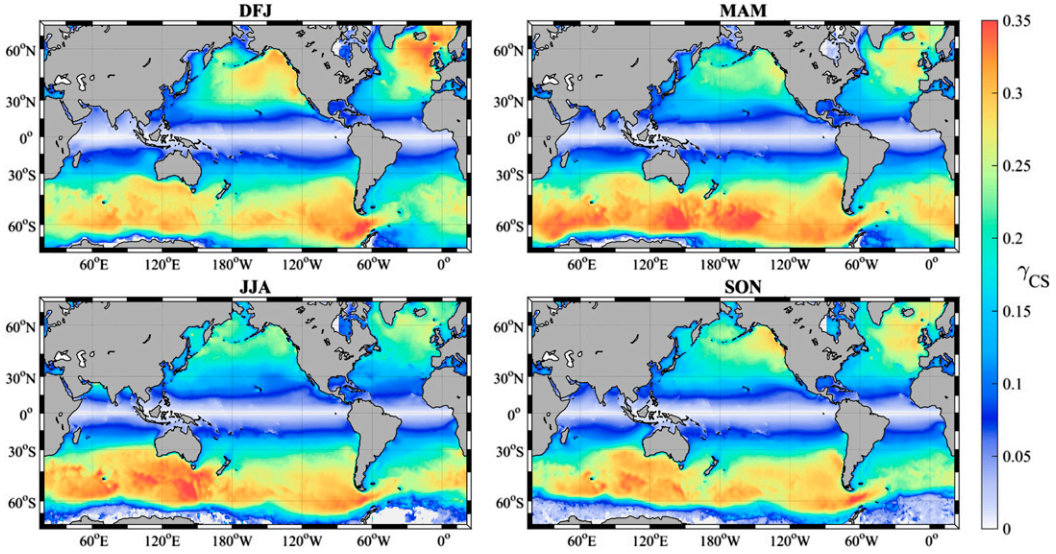

FIG. 10. As in Fig. 9, but for γ_{CS} as defined in the text by Eq. (28).

this can be rewritten using the turbulent Langmuir number $\mathrm{La} = (u_*/U_0)^{1/2}$, which scales the ratio of wind-forced production of turbulent kinetic energy (TKE) to the wave-forced production of TKE (McWilliams et al. 1997; Grant and Belcher 2009), with typical values of 0.2–0.5 (Smith 1992; Belcher et al. 2012). This suggests that $\gamma_{\mathrm{CS}} \sim O(1)$ for h_s/h_{Ek} of 0.04–0.25.

To form estimates of the global distributions of γ_{GEO} and γ_{CS}, a combination of reanalysis data and model output is utilized. The total Stokes transport is found from the WaveWatch III (WWIII) model, reported every 6 h on a 0.5° grid (Rascle et al. 2008; Rascle and Ardhuin 2013). For consistency with the WWIII model forcing, we utilize NCEP Climate Forecast System Reanalysis (CFSR) wind stress, temperature, and salinity at 5 m and horizontal currents at 5 and 15 m depth (Saha et al. 2006). To estimate the geostrophic stress, we calculate buoyancy gradients from monthly 5-m temperature and salinity (0.5° resolution) and then infer approximate monthly values of A_v using the surface boundary condition $A_v = \boldsymbol{\tau}_w(\rho\partial u/\partial z)^{-1}$, with the near-surface shear magnitude approximated using CFSR velocities at 5 and 15 m, $\partial u/\partial z \sim |\mathbf{u}(-5) - \mathbf{u}(-15)|/10$. Alternate parameterizations of A_v were tested, including wind-stress-only parameterizations (Wenegrat et al. 2014) and bulk Richardson number closures (Pollard et al. 1972), and were found to give similar results (not shown here). Monthly values of the Stokes transport and $\boldsymbol{\tau}_{\mathrm{geo}}$ over the period 2001–11 are then used to form climatologies of γ_{GEO} and γ_{CS}.

Figures 9 and 10 show the global seasonal climatology of γ_{GEO} and γ_{CS}, respectively. The dependence on latitude through the Coriolis frequency is apparent in both quantities, with γ_{GEO} peaking at low latitudes and γ_{CS} dominating at higher latitudes (Fig. 11). Regional variability is also evident, with γ_{GEO} enhanced in boundary currents, along the equatorward edges of the subtropical gyres, and through much of the Indian Ocean and eastern subtropical Pacific. These parameterized results can be compared to estimates derived from model output and alternate parameterizations of A_v, which indicate similar spatial patterns (Chu 2015; Cronin and Tozuka 2015).

In the zonal average and temporal average, γ_{CS} becomes larger than γ_{GEO} poleward of 15° (Figs. 10, 11), following a spatial pattern that in large part reflects the variability in Stokes transport (McWilliams and Restrepo 1999). This latitudinal pattern may also reflect the effect of the coarse-resolution products utilized here on estimating γ_{GEO}, as the first baroclinic Rossby radius at 15° is ~100 km (Chelton et al. 1998), which is close to the resolved meridional Nyquist wavelength, and hence ∇b may be underestimated at higher latitudes. Wide

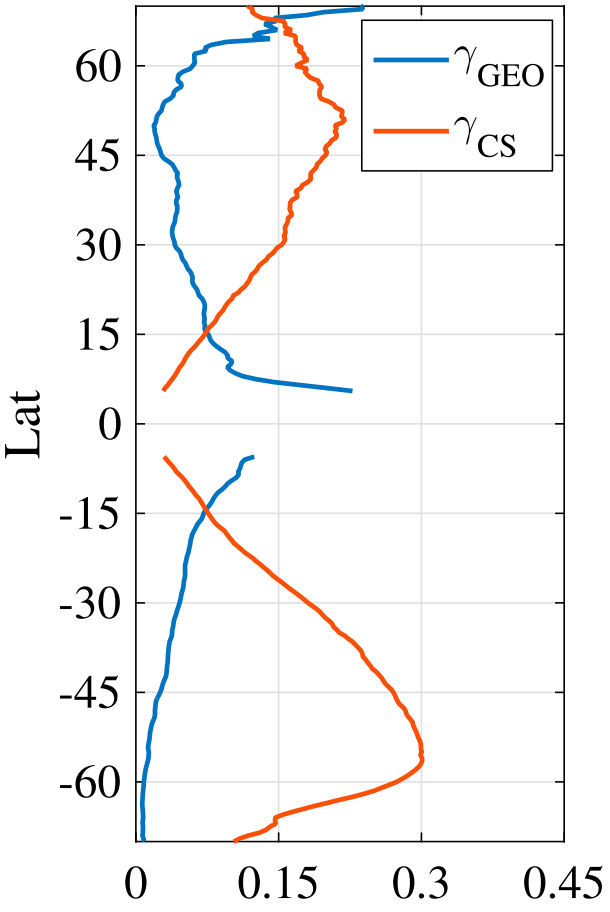

FIG. 11. Zonal and temporal averages of γ_{GEO} and γ_{CS}.

swaths of the world oceans have $\gamma_{\mathrm{CS}} \sim 0.25$, emphasizing how important these effects may be for Ekman-layer currents. Intensification of γ_{CS} in the Southern Ocean is also evident. In the Northern Hemisphere there is a general enhancement of γ_{CS} in the eastern side of the ocean basins, with seasonal variability in both extent and magnitude, resulting from enhanced Stokes transport associated with increased wintertime wind forcing.

The relative influences of the geostrophic stress and the Coriolis–Stokes stress can be considered using the joint probability density function (PDF) of the monthly estimates of γ_{GEO} and γ_{CS}, evaluated between 5° and 73.5° from 2001 to 2011 (Fig. 12). Consistent with the spatial maps, the PDF has a broad peak at $\gamma_{\mathrm{CS}} \sim 0.1$–0.25 with negligible γ_{GEO}. However, the distribution of γ_{GEO} is long-tailed, reflecting its spatial and temporal inhomogeneity, evident in comparing an example month (Fig. 13) and the climatological maps (Figs. 9, 10). Considering the total relative change in the effective surface stress arising from both the geostrophic stress and the Coriolis–Stokes stress, $\gamma_T = \gamma_{\mathrm{GEO}} + \gamma_{\mathrm{CS}}$, 36%

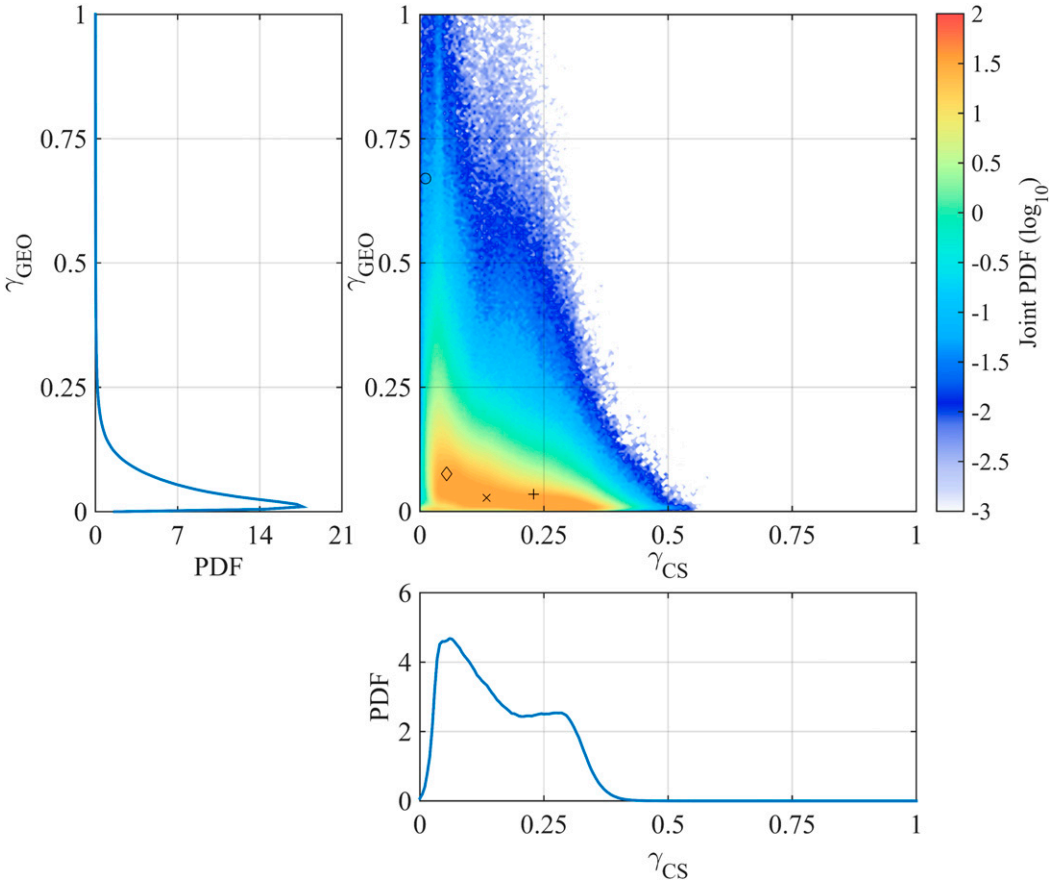

FIG. 12. Global area-weighted joint PDF of γ_{GEO} and γ_{CS} (top right) estimated monthly from 2001 to 2011. (top left) The PDF of γ_{GEO} and (bottom) the PDF of γ_{CS}. Climatological average values are indicated in the top-right panel for the locations of several previous Ekman layer studies: Long Term Upper Ocean Study (cross symbol; Price et al. 1987); Transpacific Hydrographic Survey (basin averaged, diamond symbol; Wijffels et al. 1994); Eastern Boundary Current experiment (plus sign; Chereskin 1995); and 2°N, 140°W (circle symbol; Cronin and Kessler 2009).

of all points have $\gamma_T > 0.25$. Together, the estimates presented above, while only a rough approximation, suggest that surface waves will be of $O(1)$ importance for much of the extratropics, while baroclinic pressure gradients will dominate at low latitudes, in frontal systems, and potentially over shorter time scales and smaller spatial scales than resolved here, specifically at the submesoscale, where geostrophic stress effects have been demonstrated to significantly modify the ageostrophic flow (Ponte et al. 2013; Gula et al. 2014; McWilliams et al. 2015).

b. *Horizontal fluxes*

The proceeding analysis, and theory, highlights how ocean sources of stress can be expected to modify the frictional response within the near-surface layer, affecting the magnitude, direction, and vertical profile of the ageostrophic flow. These modifications to the ageostrophic velocity can often be approximated using the concept of an effective stress $\boldsymbol{\tau}_{\text{Eff}}$ (section 3), leading to a modified Ekman velocity scale of $u_{\text{Ek}} \sim \tau_{\text{Eff}}/(\rho f h_{\text{Ek}})$. This has wide-ranging implications for horizontal advective fluxes, where, for example, the geostrophic stress will always enhance heat flux down the buoyancy gradient relative to the classic Ekman solution, as well as for other dynamically important quantities such as the wind work on the total ageostrophic flow $\boldsymbol{\tau}_w \cdot \mathbf{u}_{\text{Ek}}$, which will be reduced for winds aligned with the surface frontal jet (down-front winds) and enhanced for winds aligned against the frontal jet (up-front winds).

A brief example, which highlights the role of vertical structure in A_v, is given by considering the differential horizontal buoyancy flux across the surface Ekman layer, which can change the stratification, and hence the potential vorticity (PV), of the near-surface layer (Thomas and Ferrari 2008). A scaling for the frictional

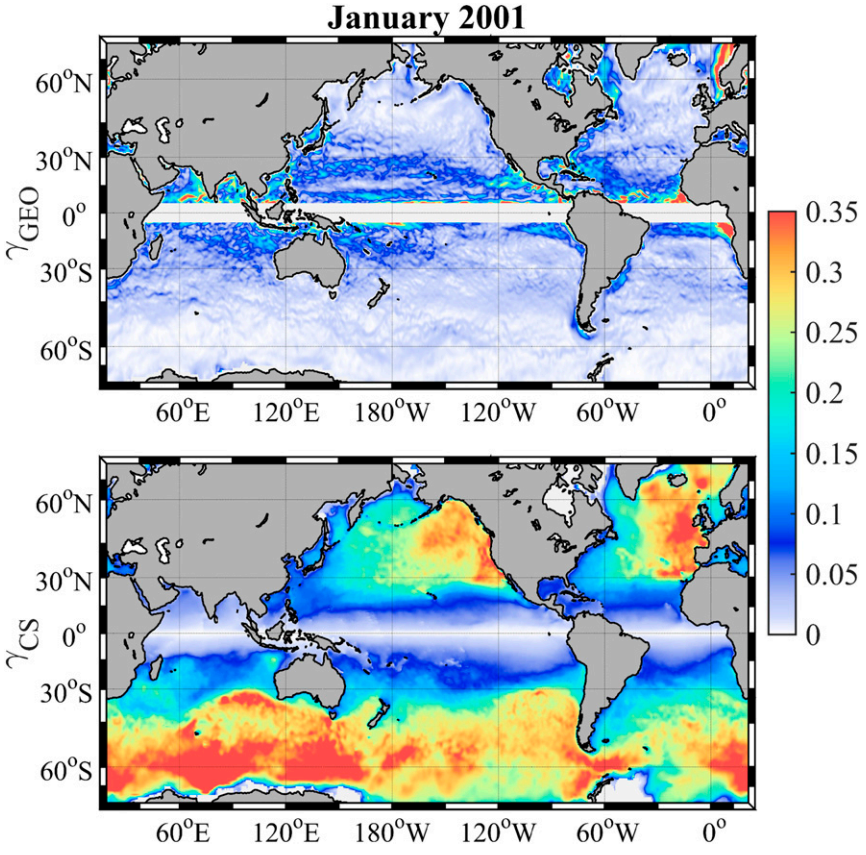

FIG. 13. Example single month estimate of γ_{GEO} and γ_{CS}, showing additional spatial detail not evident in the climatological maps (Figs. 9, 10).

flux of the vertical component of PV due to a surface wind stress aligned orthogonally to a horizontal buoyancy gradient is given by (Thomas 2005; Thomas and Ferrari 2008)

$$J_z^F \sim \frac{\tau_w}{\rho h_{\mathrm{Ek}}} \nabla b. \tag{29}$$

However, if A_v is allowed to vary vertically, with depth scale h_{A_v}, this scaling is modified to become

$$J_z^F \sim \frac{\tau_w}{\rho h_{\mathrm{Ek}}} \nabla b \left(1 + \frac{h_{\mathrm{Ek}}}{4 h_{A_v}}\right). \tag{30}$$

This relationship is shown in Fig. 14 for a wind stress aligned with the front and an exponential A_v profile that decreases (increases) $h_{A_v} > 0$ ($h_{A_v} < 0$) with depth. As $|h_{A_v}|$ approaches h_{Ek}, the surface cross-front current is enhanced (reduced) for $h_{A_v} > 0$ ($h_{A_v} < 0$), modifying the frictional PV flux. A similar result can be easily derived for the influence of the vertical structure of A_v on the frictional PV flux associated with the frontal spin-down by the geostrophic stress (Thomas and Ferrari 2008). Thus, the vertical structure of mixing is linked to the flux of vertical potential vorticity through its effect on the differential horizontal advection of buoyancy.

A conceptual example of how this might affect the ocean boundary layer is found by considering the near-surface response to up-front and down-front winds. Down-front winds advect dense water over light water, leading to gravitational instability, whereas up-front winds advect light water over dense, enhancing stratification (Thomas and Lee 2005). Making the idealization that down-front winds lead to a well-mixed layer with $A_v \sim$ constant, whereas up-front winds lead to a stratified near-surface layer with A_v decreasing with depth, would imply the existence of an asymmetry in PV fluxes between the two cases. Consequently, for the same wind stress and buoyancy gradient magnitudes, wind-driven frictional PV fluxes may be enhanced in up-front wind conditions relative to down-front winds, providing a possible alternative route to the creation of positively skewed PV distributions (Thomas 2007).

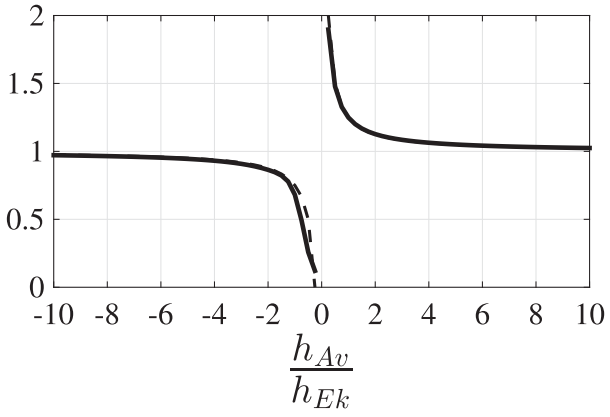

FIG. 14. Frictional flux of vertical potential vorticity due to the wind-driven differential horizontal buoyancy advection across the Ekman layer. Numerical solutions of $f[\mathbf{u}_{\mathrm{Ek}} \cdot \nabla b]_{z=0}$ are plotted (solid) as a function of the eddy viscosity depth scale, where $A_v(z) = A_{v0}e^{z/h_{Av}}$. Values are normalized by Eq. (29). Also plotted is the scaling suggested by Eq. (30) (dashed), which overlaps the numerical solution for most of the parameter space.

6. Summary

In this manuscript we present an approximate solution to the generalized Ekman (Cronin and Kessler 2009), or turbulent thermal wind (Gula et al. 2014; McWilliams et al. 2015), balance. While this theory omits many aspects of boundary layer physics that are likely to be active in the real ocean, the simplicity and generality of the solution provides a useful tool for gaining insight into the underlying dynamics beyond that available from numerical methods. The full solution, Eq. (7), given in terms of an integral over a Green's function, can be applied quite generally to a variety of sources of near-surface shear and further allows for arbitrary vertical structure in A_v, subject to the constraints imposed by the WKB method. Many existing modified Ekman theories can thus be considered as particular cases of this solution, providing a framework for comparing their effects on ageostrophic ocean currents.

Two important aspects of surface layer dynamics that are not as readily accommodated in this framework are time dependence and nonlinearity. Observations suggest significant diurnal variability of near-surface shear (Price et al. 1986; Schudlich and Price 1998; Cronin and Kessler 2009; Smyth et al. 2013; Wenegrat and McPhaden 2015), which has been suggested as an explanation of observed discrepancies with classic Ekman theory (Price and Sundermeyer 1999). However, analysis of near-surface velocity observations appears to suggest that some of the observed features that have been used to argue for the role of time variability, such as a flattened spiral, can also be very well explained by alternate mechanisms that do not invoke time dependence (Lewis and Belcher 2004; Polton et al. 2005; Cronin and Kessler 2009). Disentangling these effects using observations is further complicated by measurement challenges, particularly for moored observations that can be biased by surface waves (Rascle and Ardhuin 2009). A focus of future work should be clarifying the relative contributions of, and interactions between, the diverse sources of near-surface ageostrophic flow.

Nonlinear effects may be of particular importance in examining sharp horizontal buoyancy gradients (Stern 1965; Niiler 1969; Thomas and Rhines 2002; Mahadevan and Tandon 2006). However, a range of modeling efforts that include more complete physics indicate that the basic dynamical mechanisms discussed here continue to be of first-order importance in the boundary layer, even at high ε (Thompson 2000; Nagai et al. 2006; Ponte et al. 2013; Gula et al. 2014; McWilliams et al. 2015). We also note that the work of Wu and Blumen (1982) and Tan (2001) can be considered as a blueprint for how the semigeostrophic momentum approximation could be incorporated into the solution given here.

Examining two limiting cases, the first for Stokes shear of shallow depth relative to h_{Ek} and the second for a front much deeper than h_{Ek}, reveals the key underlying dynamics. Ocean sources of shear, in the presence of viscosity, act as sources of stress. These ocean sources of stress are, as a first approximation, independent of the surface wind stress and are capable of driving their own ageostrophic flow, including creating a surface Ekman layer. The equivalency of the closed form solutions for the two limiting cases emphasizes how robust this interpretation of the underlying dynamics is, suggesting the same interpretation holds for the more general Green's function solution [Eq. (7)] and highlighting a previously unnoted connection between the frictional effects of surface waves and fronts.

The solutions presented here are unique in their ability to incorporate arbitrary vertical structure in A_v, which is motivated physically by modeling and direct turbulence measurements (Zikanov et al. 2003; Kirincich 2013; Soloviev and Lukas 2014) and is shown here to lead to modifications of both horizontal and vertical flows. Improved understanding of the spatial variability of mixing is key to understanding and parameterizing these effects on boundary layer flow. Finally, it should be emphasized that the various dynamical processes discussed here should not be considered as the addition of new parameters to the Ekman problem, but rather as fundamental components of the frictional response of the ocean boundary layer, whose influence may be of the same order of magnitude as the surface wind stress throughout large portions of the global oceans. The total frictional ageostrophic response

is a combination of a response to the surface wind, as in the classic Ekman theory, and a response to ocean sources of shear.

Acknowledgments. We thank Leah Johnson, Hayley Dosser, and Andrew Shao for many helpful discussions during the course of this work. The comments and suggestions of two anonymous reviewers improved this manuscript. This publication is partially funded by the Joint Institute for the Study of the Atmosphere and Ocean (JISAO) under NOAA Cooperative Agreement NA10OAR4320148. WaveWatch III model output is available from the IOWAGA group at http://wwz.ifremer.fr/iowaga/Products. NCEP CFSR data are available at http://rda.ucar.edu/pub/cfsr.html.

APPENDIX A

Derivation

Let $A_v(z) = A_{v0}\psi(z)$, then, after nondimensionalizing Eq. (3) as discussed in section 2, we have

$$\mathrm{Ek}\tau'' - \frac{i}{\psi(z)}\boldsymbol{\tau} = \boldsymbol{\xi}(z), \tag{A1}$$

$$\boldsymbol{\tau}(0) = \boldsymbol{\tau}_w, \quad \text{and} \tag{A2}$$

$$\boldsymbol{\tau}(-h) = 0, \tag{A3}$$

where primes indicate vertical derivatives and all variables are nondimensional unless otherwise noted. The RHS of Eq. (A1) is given in terms of a generic inhomogeneous forcing function $\boldsymbol{\xi}(z)$, which could arise from geostrophic shear or Coriolis–Stokes shear as discussed in section 3. Solving first for the homogenous solution and making the WKB assumption,

$$\tau \propto e^{(S_0 + S_1\delta + S_2\delta^2 + \cdots)/\delta}, \tag{A4}$$

gives

$$\mathrm{Ek}\left(\frac{S_0''}{\delta} + \frac{S_0'^2}{\delta^2} + \frac{2S_0'S_1'}{\delta} + S_1'' + S_1'^2\right)\boldsymbol{\tau} - \frac{i}{\psi(z)}\boldsymbol{\tau} = 0. \tag{A5}$$

The distinguished limit for the parameter δ is therefore $\delta \sim \mathrm{Ek}^{1/2}$, and the balance conditions are given by

$$O(\delta^{-2})\text{: } S_0' = \pm\sqrt{\frac{i}{\psi(z)}}, \quad \text{and} \tag{A6}$$

$$O(\delta^{-1})\text{: } S_1' = -\frac{S_0''}{2S_0'}. \tag{A7}$$

Taking the positive root of S_0' gives

$$S_0 = \sqrt{i}\int_{-h}^{z} \psi(Z)^{-1/2}\, dZ, \tag{A8}$$

and

$$S_1 = \frac{1}{4}\log\psi(z). \tag{A9}$$

A similar argument is followed for the negative root, giving the two solutions to the ODE, which dimensionally are given by

$$\boldsymbol{\tau}(z) = C_1 \underbrace{A_v(z)^{1/4}e^{\theta(z)}}_{y_1} + C_2 \underbrace{A_v(z)^{1/4}e^{-\theta(z)}}_{y_2}, \tag{A10}$$

where

$$\theta(z) = \sqrt{if}\int_{-h}^{z} A_v(Z)^{-1/2}\, dZ. \tag{A11}$$

For the WKB approximation to hold, two conditions must be satisfied (Bender and Orszag 1978):

$$\frac{\mathrm{Ek}^{1/2}S_1}{S_0} \ll 1, \quad \mathrm{Ek}^{1/2} \to 0, \quad \text{and} \tag{A12}$$

$$\mathrm{Ek}^{1/2}S_2 \ll 1, \quad \mathrm{Ek}^{1/2} \to 0, \tag{A13}$$

discussed further in appendix B.

Variation of parameters gives the inhomogeneous portion of the solution,

$$\boldsymbol{\tau}_p = -y_1\int\frac{y_2\boldsymbol{\xi}(z)}{W(y_1,y_2)}dz + y_2\int\frac{y_1\boldsymbol{\xi}(z)}{W(y_1,y_2)}dz, \tag{A14}$$

where W is the Wronskian,

$$W(y_1,y_2) = y_1y_2' - y_2y_1' = -2\sqrt{if}. \tag{A15}$$

Thus,

$$\boldsymbol{\tau}_p = A_v(z)^{1/4}e^{\theta(z)}\int\frac{e^{-\theta(z)}A_v(z)^{1/4}\boldsymbol{\xi}(z)}{2\sqrt{if}}dz - A_v(z)^{1/4}e^{-\theta(z)}\int\frac{e^{\theta(z)}A_v(z)^{1/4}\boldsymbol{\xi}(z)}{2\sqrt{if}}dz. \tag{A16}$$

Changing the limits of integration gives

$$\boldsymbol{\tau}_p = \int_0^z \frac{\sinh[\theta(z)-\theta(s)]A_v(z)^{1/4}A_v(s)^{1/4}\boldsymbol{\xi}(s)}{\sqrt{if}}ds. \tag{A17}$$

So, the total solution, before application of the boundary conditions, is given by

$$\boldsymbol{\tau}_t(z) = C_1 A_v(z)^{1/4} e^{\theta(z)} + C_2 A_v(z)^{1/4} e^{-\theta(z)} + \int_0^z \frac{\sinh[\theta(z)-\theta(s)] A_v(z)^{1/4} A_v(s)^{1/4} \boldsymbol{\xi}(s)}{\sqrt{if}}\, ds. \tag{A18}$$

Applying the surface BC gives

$$\boldsymbol{\tau}_w = C_1 A_v(0)^{1/4} e^{\theta(0)} + C_2 A_v(0)^{1/4} e^{-\theta(0)}; \tag{A19}$$

therefore,

$$\boldsymbol{\tau}_t(z) = 2C_1 A_v(z)^{1/4} e^{\theta(0)} \sinh[\theta(z)-\theta(0)] + \boldsymbol{\tau}_w \left[\frac{A_v(z)}{A_v(0)}\right]^{1/4} e^{\theta(0)-\theta(z)} + \int_0^z \frac{\sinh[\theta(z)-\theta(s)] A_v(z)^{1/4} A_v(s)^{1/4} \boldsymbol{\xi}(s)}{\sqrt{if}}\, ds. \tag{A20}$$

The lower BC gives

$$0 = 2C_1 A_v(-h)^{1/4} e^{\theta(0)} \sinh[\theta(-h)-\theta(0)] + \boldsymbol{\tau}_w \left[\frac{A_v(-h)}{A_v(0)}\right]^{1/4} e^{\theta(0)-\theta(-h)} + \int_0^{-h} \frac{\sinh[\theta(-h)-\theta(s)] A_v(-h)^{1/4} A_v(s)^{1/4} \boldsymbol{\xi}(s)}{\sqrt{if}}\, ds. \tag{A21}$$

Following Hidaka (1955), we multiply Eq. (A20) by $\sinh[-\theta(0)]$, Eq. (A21) by $-[A_v(z)/A_v(-h)]^{1/4} \sinh[\theta(z)-\theta(0)]$, and add them, giving

$$\boldsymbol{\tau}(z) = \boldsymbol{\tau}_w \left[\frac{A_v(z)}{A_v(0)}\right]^{1/4} \frac{\sinh[\theta(z)]}{\sinh[\theta(0)]} + \int_0^z \frac{\sinh[\theta(z)-\theta(s)] \sinh[\theta(0)] \boldsymbol{\xi}(s) A_v(s)^{1/4} A_v(z)^{1/4}}{\sqrt{if} \sinh[\theta(0)]}\, ds - \int_0^{-h} \frac{\sinh[\theta(z)-\theta(0)] \sinh[\theta(s)] \boldsymbol{\xi}(s) A_v(s)^{1/4} A_v(z)^{1/4}}{\sqrt{if} \sinh[\theta(0)]}\, ds. \tag{A22}$$

This can be rewritten as

$$\boldsymbol{\tau}(z) = \boldsymbol{\tau}_w \left[\frac{A_v(z)}{A_v(0)}\right]^{1/4} \frac{\sinh[\theta(z)]}{\sinh[\theta(0)]} + \int_{-h}^0 G(z,s) \boldsymbol{\xi}(s)\, ds, \tag{A23}$$

$$\theta(z) = \sqrt{if} \int_{-h}^z A_v(Z)^{-1/2}\, dZ, \tag{A24}$$

$$G(z,s) = \begin{cases} \dfrac{\sinh[\theta(z)] \sinh[\theta(s)-\theta(0)] A_v(s)^{1/4} A_v(z)^{1/4}}{\sinh[\theta(0)] \sqrt{if}} & \text{if} \quad s > z \\ \dfrac{\sinh[\theta(s)] \sinh[\theta(z)-\theta(0)] A_v(s)^{1/4} A_v(z)^{1/4}}{\sinh[\theta(0)] \sqrt{if}} & \text{if} \quad s < z. \end{cases} \tag{A25}$$

APPENDIX B

Accuracy of Approximate Solution

The validity of the physical-optics WKB approximation requires the criteria Eqs. (A12) and (A13) be satisfied (Bender and Orszag 1978). The relative error in the approximation will then be a function of the small parameter $\delta \sim \mathrm{Ek}^{1/2}$ and the first ignored term S_2 in Eq. (A4), which involves both first and second derivatives of A_v. Thus, errors will be a function of the Ekman number Ek, as well as the particular vertical structure of A_v. Anecdotally, the WKB solution Eq. (7) has proven extremely accurate across a wide range of vertical structures of A_v and values of Ek considered in developing the model (see also Grisogono 1995; Berger and Grisogono 1998). However, to better illustrate the accuracy of the approximate solution, we consider the

relative error associated with three idealized forms of A_v (Fig. B1). In each case the normalization is such that $h = 1, f = 1$, and $A_{v0} = \mathrm{Ek} \times 1\,\mathrm{m^2\,s^{-1}}$.

Case I is a simple exponentially decaying profile,

$$A_v(z) = A_{v0} e^{\hat{z}/0.125}, \tag{B1}$$

chosen for its analytic simplicity and consistency with observations (Peters et al. 1988; Dillon et al. 1989). Case II is a linearly decaying profile,

$$A_v(z) = A_{v0}\left(1 + \frac{\hat{z}}{1+\mu}\right), \tag{B2}$$

where μ is a small value added to avoid a singularity at $z = -1$. Case III is a modified Gaussian profile (Parmhed et al. 2005),

$$A_v(z) = A_{v0}\phi\hat{z}e^{-0.5(\hat{z}/0.25)^2} + \mu, \tag{B3}$$

where $\phi = 4e^{1/2}$, which approximates the polynomial profile of O'Brien (1970), and μ is a small parameter added for computational regularity (e.g., McWilliams and Huckle 2006). The results of the error analysis are not dependent on the value of μ, which we take to be $\mu = 10^{-6}\,\mathrm{m^2\,s^{-1}}$. This profile violates Eq. (A12) in a thin layer near $\hat{z} = 0$, where $A_v \to \mu$, and hence the WKB solution must be patched to an inner solution valid in this thin near-surface region. The depth at which the patching occurs z_p can be determined following Parmhed et al. (2005) as

$$z_p = -\frac{1}{4}\left[W\left(\frac{2}{\sqrt{\phi}}\right)\right]^2, \tag{B4}$$

where W is the Lambert W function (Corless et al. 1996). For the values used here, $z_p = -0.06$. For the case of a surface wind stress, an appropriate inner solution is determined by assuming a linearized eddy viscosity, $A_{vl}(\hat{z}) = \phi|\hat{z}| + \mu$, valid for $\hat{z} \to 0$, giving (Madsen 1977)

$$\boldsymbol{\tau}_{\mathrm{Inner}} = \boldsymbol{\tau}_w \frac{\sqrt{\beta(z)}}{\sqrt{\beta(0)}} \frac{K_1[2\sqrt{\beta(z)}]}{K_1[2\sqrt{\beta(0)}]}, \tag{B5}$$

where $\beta(z) = [ifA_{vl}(\hat{z})]/\phi^2$ and K_1 is the first-order modified Bessel function of the second kind (Abramowitz and Stegun 1964). This solution is then patched to the WKB solution at $\hat{z} = z_p$.

Determining the appropriate patched solution for the inhomogeneous problem is beyond the scope of the present work. Thus, for assessing the error associated with geostrophic stress forcing, we make the simplifying approximation of applying the surface boundary condition directly to the WKB solution at z_p, similar to the introduction of a roughness length scale (Madsen 1977), and equivalent in the error analysis to the requirement that any inner solution be exact. The validity of this approximation is supported by the accuracy of the patched homogeneous solution (Fig. B2), which suggests that an appropriate inner solution for the inhomogeneous problem could be identified using variation of parameters (appendix A).

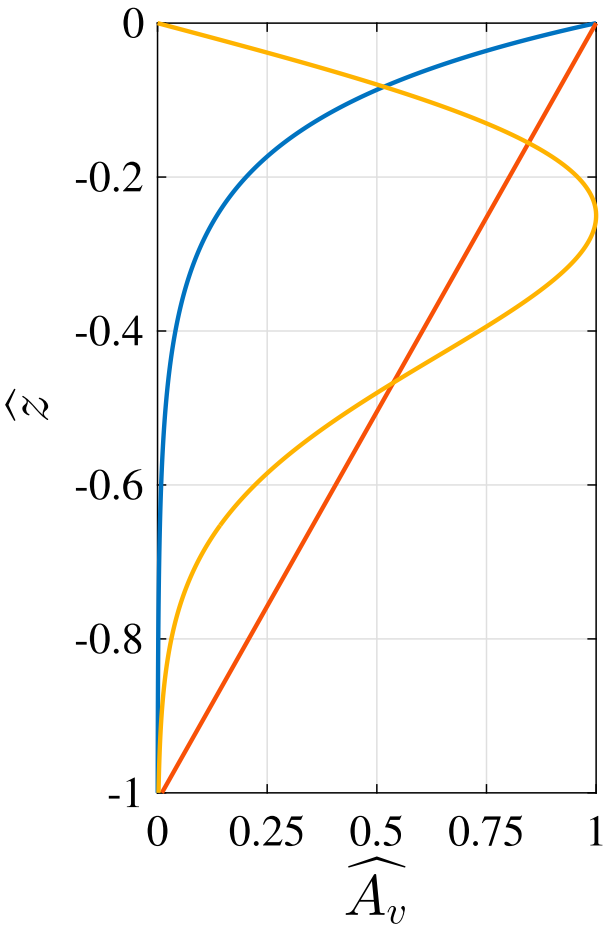

FIG. B1. Vertical structure of A_v models considered in appendix B.

To form an estimate of the relative error as a function of Ek, WKB solutions [Eq. (7)] are compared to numeric solutions, found using a shooting method, and the normalized maximum error identified in each vertical profile,

$$\widehat{\tau_{\mathrm{err}}}(\mathrm{Ek}) = \frac{\max\{|\tau_{\mathrm{WKB}}(z,\mathrm{Ek}) - \tau_{\mathrm{num}}(z,\mathrm{Ek})|\}}{\max\{|\tau_{\mathrm{num}}(z,\mathrm{Ek})|\}}. \tag{B6}$$

Results are plotted in Fig. B2 for the patched solution with wind stress forcing (top) and solutions forced by a vertically uniform buoyancy gradient (bottom). Also

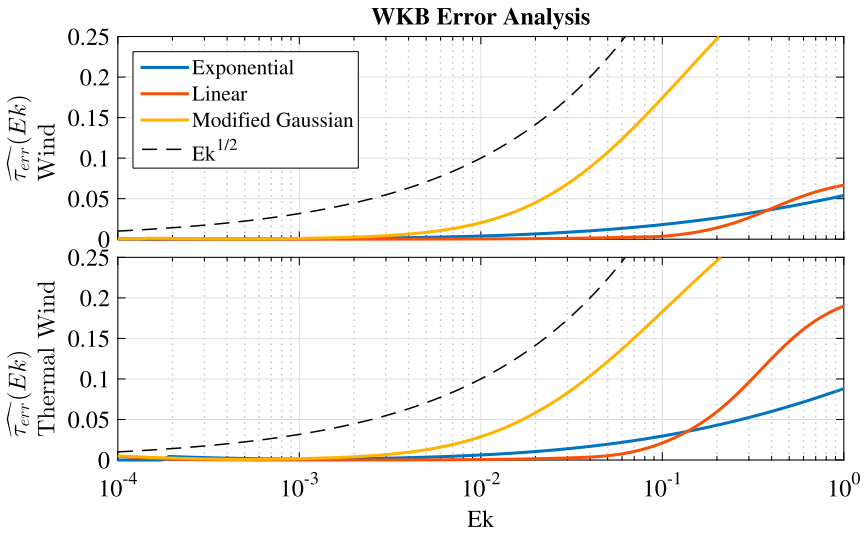

FIG. B2. Accuracy of WKB approximation as a function of Ekman number for the A_v profiles shown in Fig. B1: (top) for wind forcing and (bottom panel) for a vertically uniform horizontal buoyancy gradient. Errors are normalized according to Eq. (B6).

plotted for reference is the value of the small parameter $\delta \sim \mathrm{Ek}^{1/2}$. Errors are generally small and, for $\mathrm{Ek} \leq 10^{-1}$, the only case with relative errors exceeding 5% is the modified exponential profile, Eq. (B3). The errors associated with this profile are strongly dependent on the choice of patching depth z_p rather than the overall vertical structure, as can be anticipated through the logarithmic singularity evident in Eq. (A12). Hence, caution is required in applying Eq. (7) in cases where $A_v \rightarrow 0$ near a boundary.

REFERENCES

Abramowitz, M., and I. A. Stegun, Eds., 1964: *Handbook of Mathematical Functions: With Formulas, Graphs, and Mathematical Table*s. Dover Books on Mathematics, Dover Publications, 1046 pp.

Aiki, H., and R. J. Greatbatch, 2012: Thickness-weighted mean theory for the effect of surface gravity waves on mean flows in the upper ocean. *J. Phys. Oceanogr.*, **42**, 725–747, doi:10.1175/JPO-D-11-095.1.

Belcher, S. E., and Coauthors, 2012: A global perspective on Langmuir turbulence in the ocean surface boundary layer: FRONTIER. *Geophys. Res. Lett.*, **39**, L18605, doi:10.1029/2012GL052932.

Bender, C. M., and S. A. Orszag, 1978: *Advanced Mathematical Methods for Scientists and Engineers.* Springer, 593 pp.

Berger, B. W., and B. Grisogono, 1998: The baroclinic, variable eddy viscosity Ekman layer. *Bound.-Layer Meteor.*, **87**, 363–380, doi:10.1023/A:1001076030166.

Boccaletti, G., R. Ferrari, and B. Fox-Kemper, 2007: Mixed layer instabilities and restratification. *J. Phys. Oceanogr.*, **37**, 2228–2250, doi:10.1175/JPO3101.1.

Bonjean, F., and G. S. E. Lagerloef, 2002: Diagnostic model and analysis of the surface currents in the tropical Pacific Ocean. *J. Phys. Oceanogr.*, **32**, 2938–2954, doi:10.1175/1520-0485(2002)032<2938:DMAAOT>2.0.CO;2.

Buckingham, E., 1914: On physically similar systems; Illustrations of the use of dimensional equations. *Phys. Rev.*, **4**, 345–376, doi:10.1103/PhysRev.4.345.

Caldwell, D. R., C. W. Van Atta, and K. N. Helland, 1972: A laboratory study of the turbulent Ekman layer. *Geophys. Fluid Dyn.*, **3**, 125–160, doi:10.1080/03091927208236078.

Chelton, D. B., R. A. deSzoeke, M. G. Schlax, K. El Naggar, and N. Siwertz, 1998: Geographical variability of the first baroclinic Rossby radius of deformation. *J. Phys. Oceanogr.*, **28**, 433–460, doi:10.1175/1520-0485(1998)028<0433:GVOTFB>2.0.CO;2.

Chereskin, T. K., 1995: Direct evidence for an Ekman balance in the California Current. *J. Geophys. Res.*, **100**, 18 261–18 269, doi:10.1029/95JC02182.

——, and D. Roemmich, 1991: A comparison of measured and wind-derived Ekman transport at 11°N in the Atlantic Ocean. *J. Phys. Oceanogr.*, **21**, 869–878, doi:10.1175/1520-0485(1991)021<0869:ACOMAW>2.0.CO;2.

Chu, P. C., 2015: Ekman spiral in a horizontally inhomogeneous ocean with varying eddy viscosity. *Pure Appl. Geophys.*, **172**, 2831–2857, doi:10.1007/s00024-015-1063-4.

Corless, R. M., G. H. Gonnet, D. E. G. Hare, D. J. Jeffrey, and D. E. Knuth, 1996: On the Lambert W function. *Adv. Comput. Math.*, **5**, 329–359, doi:10.1007/BF02124750.

Cronin, M. F., and W. S. Kessler, 2009: Near-surface shear flow in the tropical Pacific cold tongue front. *J. Phys. Oceanogr.*, **39**, 1200–1215, doi:10.1175/2008JPO4064.1.

——, and T. Tozuka, 2015: Ekman ocean response to wind forcing in extratropical frontal regions. *19th Conf. on Air–Sea Interaction*, Phoenix, AZ, Amer. Meteor. Soc., 6.4. [Available online at https://ams.confex.com/ams/95Annual/webprogram/Paper267544.html.]

Csanady, G., 1982: Frictional secondary circulation near an upwelled thermocline. Tech. Rep. WHOI-82-52, Woods Hole Oceanographic Institution, 56 pp.

Dewey, R. K., and J. N. Moum, 1990: Enhancement of fronts by vertical mixing. *J. Geophys. Res.*, **95**, 9433–9445, doi:10.1029/JC095iC06p09433.

Dillon, T. M., J. N. Moum, T. K. Chereskin, and D. R. Caldwell, 1989: Zonal momentum balance at the equator. *J. Phys. Oceanogr.*, **19**, 561–570, doi:10.1175/1520-0485(1989)019<0561:ZMBATE>2.0.CO;2.

Ekman, V., 1905: On the influence of the earth's rotation on ocean currents. *Ark. Mat. Astron. Fys.*, **2**, 1–53.

Elipot, S., and S. T. Gille, 2009: Ekman layers in the Southern Ocean: Spectral models and observations, vertical viscosity and boundary layer depth. *Ocean Sci.*, **5**, 115–139, doi:10.5194/os-5-115-2009.

Garrett, C. J. R., and J. W. Loder, 1981: Dynamical aspects of shallow sea fronts. *Philos. Trans. Roy. Soc. London*, **A302**, 563–581, doi:10.1098/rsta.1981.0183.

Gill, A. E., 1982: *Atmosphere-Ocean Dynamics*. International Geophysics Series, Vol. 30, Academic Press, 662 pp.

Grant, A. L. M., and S. E. Belcher, 2009: Characteristics of Langmuir turbulence in the ocean mixed layer. *J. Phys. Oceanogr.*, **39**, 1871–1887, doi:10.1175/2009JPO4119.1.

Grisogono, B., 1995: A generalized Ekman layer profile with gradually varying eddy diffusivities. *Quart. J. Roy. Meteor. Soc.*, **121**, 445–453, doi:10.1002/qj.49712152211.

Gula, J., M. J. Molemaker, and J. C. McWilliams, 2014: Submesoscale cold filaments in the Gulf Stream. *J. Phys. Oceanogr.*, **44**, 2617–2643, doi:10.1175/JPO-D-14-0029.1.

Hidaka, K., 1955: Wind circulation in a two-layer zonal ocean. *Japan. J. Geophys*, **1**, 2.

Huang, N. E., 1971: Derivation of Stokes drift for a deep-water random gravity wave field. *Deep-Sea Res. Oceanogr. Abstr.*, **18**, 255–259, doi:10.1016/0011-7471(71)90115-X.

——, 1979: On surface drift currents in the ocean. *J. Fluid Mech.*, **91**, 191–208, doi:10.1017/S0022112079000112.

Jenkins, A. D., 1986: A theory for steady and variable wind-and wave-induced currents. *J. Phys. Oceanogr.*, **16**, 1370–1377, doi:10.1175/1520-0485(1986)016<1370:ATFSAV>2.0.CO;2.

Kirincich, A. R., 2013: Long-term observations of turbulent Reynolds stresses over the inner continental shelf. *J. Phys. Oceanogr.*, **43**, 2752–2771, doi:10.1175/JPO-D-12-0153.1.

Komen, G. J., L. Vavaleri, M. Donelan, K. Hasselmann, S. Hasselmann, and P. A. E. M. Janssen, 1996: *Dynamics and Modelling* of *Ocean Waves*. 1st ed., Cambridge University Press, 556 pp.

Large, W. G., J. C. McWilliams, and S. C. Doney, 1994: Oceanic vertical mixing: A review and a model with a nonlocal boundary layer parameterization. *Rev. Geophys.*, **32**, 363–403, doi:10.1029/94RG01872.

Lewis, D., and S. Belcher, 2004: Time-dependent, coupled, Ekman boundary layer solutions incorporating Stokes drift. *Dyn. Atmos. Oceans*, **37**, 313–351, doi:10.1016/j.dynatmoce.2003.11.001.

Lupini, R., A. Speranza, and A. Trevisan, 1975: A re-examination of the classical formulation of turbulent Ekman boundary layer flow. *Nuovo Cimento*, **25B**, 871–881, doi:10.1007/BF02724758.

Madsen, O. S., 1977: A realistic model of the wind-induced Ekman boundary layer. *J. Phys. Oceanogr.*, **7**, 248–255, doi:10.1175/1520-0485(1977)007<0248:ARMOTW>2.0.CO;2.

Mahadevan, A., and A. Tandon, 2006: An analysis of mechanisms for submesoscale vertical motion at ocean fronts. *Ocean Modell.*, **14**, 241–256, doi:10.1016/j.ocemod.2006.05.006.

McPhaden, M. J., 1981: Continuously stratified models of the steady-state equatorial ocean. *J. Phys. Oceanogr.*, **11**, 337–354, doi:10.1175/1520-0485(1981)011<0337:CSMOTS>2.0.CO;2.

McWilliams, J. C., and J. M. Restrepo, 1999: The wave-driven ocean circulation. *J. Phys. Oceanogr.*, **29**, 2523–2540, doi:10.1175/1520-0485(1999)029<2523:TWDOC>2.0.CO;2.

——, and E. Huckle, 2006: Ekman layer rectification. *J. Phys. Oceanogr.*, **36**, 1646–1659, doi:10.1175/JPO2912.1.

——, and B. Fox-Kemper, 2013: Oceanic wave-balanced surface fronts and filaments. *J. Fluid Mech.*, **730**, 464–490, doi:10.1017/jfm.2013.348.

——, P. P. Sullivan, and C.-H. Moeng, 1997: Langmuir turbulence in the ocean. *J. Fluid Mech.*, **334**, 1–30, doi:10.1017/S0022112096004375.

——, E. Huckle, and A. F. Shchepetkin, 2009: Buoyancy effects in a stratified Ekman layer. *J. Phys. Oceanogr.*, **39**, 2581–2599, doi:10.1175/2009JPO4130.1.

——, ——, J.-H. Liang, and P. P. Sullivan, 2012: The wavy Ekman layer: Langmuir circulations, breaking waves, and Reynolds stress. *J. Phys. Oceanogr.*, **42**, 1793–1816, doi:10.1175/JPO-D-12-07.1.

——, ——, ——, and ——, 2014: Langmuir turbulence in swell. *J. Phys. Oceanogr.*, **44**, 870–890, doi:10.1175/JPO-D-13-0122.1.

——, J. Gula, M. J. Molemaker, L. Renault, and A. F. Shchepetkin, 2015: Filament frontogenesis by boundary layer turbulence. *J. Phys. Oceanogr.*, **45**, 1988–2005, doi:10.1175/JPO-D-14-0211.1.

Miles, J., 1994: Analytical solutions for the Ekman layer. *Bound.-Layer Meteor.*, **67**, 1–10, doi:10.1007/BF00705505.

Nagai, T., A. Tandon, and D. L. Rudnick, 2006: Two-dimensional ageostrophic secondary circulation at ocean fronts due to vertical mixing and large-scale deformation. *J. Geophys. Res.*, **111**, C09038, doi:10.1029/2005JC002964.

Niiler, P. P., 1969: On the Ekman divergence in an oceanic jet. *J. Geophys. Res.*, **74**, 7048–7052, doi:10.1029/JC074i028p07048.

O'Brien, J. J., 1970: A note on the vertical structure of the eddy exchange coefficient in the planetary boundary layer. *J. Atmos. Sci.*, **27**, 1213–1215, doi:10.1175/1520-0469(1970)027<1213:ANOTVS>2.0.CO;2.

Parmhed, O., I. Kos, and B. Grisogono, 2005: An improved Ekman layer approximation for smooth eddy diffusivity profiles. *Bound.-Layer Meteor.*, **115**, 399–407, doi:10.1007/s10546-004-5940-0.

Peters, H., M. C. Gregg, and J. M. Toole, 1988: On the parameterization of equatorial turbulence. *J. Geophys. Res.*, **93**, 1199–1218, doi:10.1029/JC093iC02p01199.

Pollard, R. T., and L. A. Regier, 1992: Vorticity and vertical circulation at an ocean front. *J. Phys. Oceanogr.*, **22**, 609–625, doi:10.1175/1520-0485(1992)022<0609:VAVCAA>2.0.CO;2.

——, P. B. Rhines, and R. O. R. Y. Thompson, 1972: The deepening of the wind-mixed layer. *Geophys. Fluid Dyn.*, **4**, 381–404, doi:10.1080/03091927208236105.

Polton, J. A., D. M. Lewis, and S. E. Belcher, 2005: The role of wave-induced Coriolis–Stokes forcing on the wind-driven mixed layer. *J. Phys. Oceanogr.*, **35**, 444–457, doi:10.1175/JPO2701.1.

——, Y.-D. Lenn, S. Elipot, T. K. Chereskin, and J. Sprintall, 2013: Can Drake Passage observations match Ekman's classic theory? *J. Phys. Oceanogr.*, **43**, 1733–1740, doi:10.1175/JPO-D-13-034.1.

Ponte, A. L., P. Klein, X. Capet, P.-Y. Le Traon, B. Chapron, and P. Lherminier, 2013: Diagnosing surface mixed layer dynamics from high-resolution satellite observations: Numerical insights. *J. Phys. Oceanogr.*, **43**, 1345–1355, doi:10.1175/JPO-D-12-0136.1.

Price, J. F., and M. A. Sundermeyer, 1999: Stratified Ekman layers. *J. Geophys. Res.*, **104**, 20 467–20 494, doi:10.1029/1999JC900164.

——, R. A. Weller, and R. Pinkel, 1986: Diurnal cycling: Observations and models of the upper ocean response to diurnal heating, cooling, and wind mixing. *J. Geophys. Res.*, **91**, 8411–8427, doi:10.1029/JC091iC07p08411.

——, ——, and R. R. Schudlich, 1987: Wind-driven ocean currents and Ekman transport. *Science*, **238**, 1534–1538, doi:10.1126/science.238.4833.1534.

Rascle, N., and F. Ardhuin, 2009: Drift and mixing under the ocean surface revisited: Stratified conditions and model-data comparisons. *J. Geophys. Res.*, **114**, C02016, doi:10.1029/2007JC004466.

——, and ——, 2013: A global wave parameter database for geophysical applications. Part 2: Model validation with improved source term parameterization. *Ocean Modell.*, **70**, 174–188, doi:10.1016/j.ocemod.2012.12.001.

——, ——, P. Queffeulou, and D. Croiz-Fillon, 2008: A global wave parameter database for geophysical applications. Part 1: Wave-current–turbulence interaction parameters for the open ocean based on traditional parameterizations. *Ocean Modell.*, **25**, 154–171, doi:10.1016/j.ocemod.2008.07.006.

Roach, C. J., H. E. Phillips, N. L. Bindoff, and S. R. Rintoul, 2015: Detecting and characterizing Ekman currents in the Southern Ocean. *J. Phys. Oceanogr.*, **45**, 1205–1223, doi:10.1175/JPO-D-14-0115.1.

Rudnick, D. L., 1996: Intensive surveys of the Azores Front: 2. Inferring the geostrophic and vertical velocity fields. *J. Geophys. Res.*, **101**, 16 291–16 303, doi:10.1029/96JC01144.

Saha, S., and Coauthors, 2006: The NCEP Climate Forecast System. *J. Climate*, **19**, 3483–3517, doi:10.1175/JCLI3812.1.

Samelson, R. M., 1993: Linear instability of a mixed-layer front. *J. Geophys. Res.*, **98**, 10 195–10 204, doi:10.1029/93JC00457.

Schudlich, R. R., and J. F. Price, 1998: Observations of seasonal variation in the Ekman layer. *J. Phys. Oceanogr.*, **28**, 1187–1204, doi:10.1175/1520-0485(1998)028<1187:OOSVIT>2.0.CO;2.

Smith, J. A., 1992: Observed growth of Langmuir circulation. *J. Geophys. Res.*, **97**, 5651–5664, doi:10.1029/91JC03118.

Smyth, W. D., J. N. Moum, L. Li, and S. A. Thorpe, 2013: Diurnal shear instability, the descent of the surface shear layer, and the deep cycle of equatorial turbulence. *J. Phys. Oceanogr.*, **43**, 2432–2455, doi:10.1175/JPO-D-13-089.1.

Soloviev, A., and R. Lukas, 2014: *The Near-Surface Layer of the Ocean: Structure, Dynamics and Applications*. 2nd ed. Atmospheric and Oceanographic Sciences Library, Vol. 48, Springer, 552 pp.

Song, J.-B., and Y.-S. Huang, 2011: An approximate solution of wave-modified Ekman current for gradually varying eddy viscosity. *Deep-Sea Res. I*, **58**, 668–676, doi:10.1016/j.dsr.2011.04.001.

Stern, M. E., 1965: Interaction of a uniform wind stress with a geostrophic vortex. *Deep-Sea Res. Oceanogr. Abstr.*, **12**, 355–367, doi:10.1016/0011-7471(65)90007-0.

Stommel, H., 1960: Wind-drift near the equator. *Deep-Sea Res.*, **6**, 298–302, doi:10.1016/0146-6313(59)90088-7.

Sullivan, P. P., and J. C. McWilliams, 2010: Dynamics of winds and currents coupled to surface waves. *Annu. Rev. Fluid Mech.*, **42**, 19–42, doi:10.1146/annurev-fluid-121108-145541.

Tan, Z.-M., 2001: An approximate analytical solution for the baroclinic and variable eddy diffusivity semi-geostrophic Ekman boundary layer. *Bound.-Layer Meteor.*, **98**, 361–385, doi:10.1023/A:1018708726112.

Thomas, L. N., 2005: Destruction of potential vorticity by winds. *J. Phys. Oceanogr.*, **35**, 2457–2466, doi:10.1175/JPO2830.1.

——, 2007: Dynamical constraints on the extreme low values of the potential vorticity in the ocean. *Extreme Events: Proc. 'Aha Huliko'a Hawaiian Winter Workshop*, Honolulu, HI, University of Hawai'i at Mānoa, 117–124. [Available online at https://pangea.stanford.edu/~leift/Thomas_Aha_2007.pdf.]

——, and P. B. Rhines, 2002: Nonlinear stratified spin-up. *J. Fluid Mech.*, **473**, 211–244, doi:10.1017/S0022112002002367.

——, and C. M. Lee, 2005: Intensification of ocean fronts by downfront winds. *J. Phys. Oceanogr.*, **35**, 1086–1102, doi:10.1175/JPO2737.1.

——, and R. Ferrari, 2008: Friction, frontogenesis, and the stratification of the surface mixed layer. *J. Phys. Oceanogr.*, **38**, 2501–2518, doi:10.1175/2008JPO3797.1.

Thompson, L., 2000: Ekman layers and two-dimensional frontogenesis in the upper ocean. *J. Geophys. Res.*, **105**, 6437–6451, doi:10.1029/1999JC900336.

Welander, P., 1957: Wind action on a shallow sea: Some generalizations of Ekman's theory. *Tellus*, **9A**, 45–52, doi:10.1111/j.2153-3490.1957.tb01852.x.

Wenegrat, J. O., and M. J. McPhaden, 2015: Dynamics of the surface layer diurnal cycle in the equatorial Atlantic Ocean (0°, 23°W). *J. Geophys. Res. Oceans*, **120**, 563–581, doi:10.1002/2014JC010504.

——, ——, and R.-C. Lien, 2014: Wind stress and near-surface shear in the equatorial Atlantic Ocean. *Geophys. Res. Lett.*, **41**, 1226–1231, doi:10.1002/2013GL059149.

Wijffels, S., E. Firing, and H. Bryden, 1994: Direct observations of the Ekman balance at 10°N in the Pacific. *J. Phys. Oceanogr.*, **24**, 1666–1679, doi:10.1175/1520-0485(1994)024<1666:DOOTEB>2.0.CO;2.

Wu, R., and W. Blumen, 1982: An analysis of Ekman boundary layer dynamics incorporating the geostrophic momentum approximation. *J. Atmos. Sci.*, **39**, 1774–1782, doi:10.1175/1520-0469(1982)039<1774:AAOEBL>2.0.CO;2.

Xu, Z., and A. J. Bowen, 1994: Wave-and wind-driven flow in water of finite depth. *J. Phys. Oceanogr.*, **24**, 1850–1866, doi:10.1175/1520-0485(1994)024<1850:WAWDFI>2.0.CO;2.

Zikanov, O., D. N. Slinn, and M. R. Dhanak, 2003: Large-eddy simulations of the wind-induced turbulent Ekman layer. *J. Fluid Mech.*, **495**, 343–368, doi:10.1017/S0022112003006244.